J. Fluid Mech. (2011), *vol.* 673, *pp.* 432–467. © Cambridge University Press 2011
doi:10.1017/S0022112010006348

Entry, start up and stability effects in visco-plastically lubricated pipe flows

S. HORMOZI[1], K. WIELAGE-BURCHARD[2] AND I. A. FRIGAARD[1,2]†

[1]Department of Mechanical Engineering, University of British Columbia, 2054-6250 Applied Science Lane, Vancouver, BC V6T 1Z4, Canada

[2]Department of Mathematics, University of British Columbia, 1984 Mathematics Road, Vancouver, BC V6T 1Z2, Canada

(Received 11 May 2010; revised 26 September 2010; accepted 6 December 2010; first published online 10 March 2011)

Interfacial instabilities of multi-layer shear flows may be eliminated by astute positioning of yield stress fluid layers that remain unyielded at the interface(s). We study the initiation, development lengths and temporal stability of such flows in the setting of a Newtonian core fluid surrounded by a Bingham lubricated fluid, within a pipe. Flow initiation is effected by starting the flow with a pipe full of stationary Bingham fluid and injecting both inner and outer fluids simultaneously. Initial instability and dispersive mixing at the front remains localised and is advected from the pipe leaving behind a stable multi-layer configuration, found for moderate Reynolds numbers (Re), for a broad range of interface radii (r_i) and for different inlet diameters (R_i), whenever the base flow parameters admit a multi-layer flow with unyielded interface. The established flows have three distinct entry lengths. These relate to: (i) establishment of the first unyielded plug close to the interface (shortest); (ii) establishment of the interface radius; (iii) establishment of the velocity profile (longest). The three entry lengths increase with Re and decrease with both the Bingham number (B) and the viscosity ratio (m). Nonlinear temporal stability to axisymmetric perturbations is studied numerically, considering initial perturbations that are either localised in yielded parts of the flow or that initially break the unyielded plug regions. The aim is to understand structural aspects of the flow stability, not easily extracted from the energy stability results of Moyers-Gonzalez, Frigaard & Nouar (*J. Fluid Mech.*, vol. 506, 2004, p. 117). The initial stages of a stable perturbed flow are characterised by a very rapid decay of the perturbation kinetic energy during which time the unyielded plug reforms (or breaks and reforms). This is followed by slower exponential decay on a viscous timescale ($t \sim Re$). For smaller Re and moderate initial amplitudes A, the perturbations decay to the numerical tolerance. As either Re or A is increased sufficiently, a number of interesting phenomena arise. The amount of dispersion increases, making the interfacial region increasingly diffuse and limiting the final decay. At larger Re or A, we find secondary flow structures that persist. A first example of these is when the shear stress decays below the yield stress before the velocity perturbation has decayed, leading to *freezing in* of the interface shape. This can lead to flows with a rigid wavy interface. Secondly, depending on the core fluid radius and thickness of the surrounding plug region, we may observe a range of dispersive structures akin to the pearls and mushrooms of d'Olce *et al.* (*Phys. Fluids*, vol. 20, 2008, art. 024104).

† Email address for correspondence: frigaard@math.ubc.ca

https://doi.org/10.1017/S0022112010006348 Published online by Cambridge University Press

Key words: core–annular flow, instability control, non-Newtonian flows

1. Introduction

Multi-layer flows occur industrially in three main settings. Firstly, there are co-extrusion processes, where a product is made of more than one layer simultaneously. Secondly, there are film coating processes, where a layer is applied to a fluid substrate. Thirdly, there are lubricated transport processes, where a lubricating fluid lies in a layer between the wall of a duct and the transported fluid. In all three processes, the flow rate (or production rate) is frequently limited by the growth of interfacial instabilities. Methodologies to suppress or eliminate interfacial instabilities and further stabilise multi-layer flows are therefore of considerable practical interest.

In this paper, we continue our study of one such method that uses a visco-plastic fluid as the lubricating fluid. The unique feature of a visco-plastic fluid is that it possesses a yield stress. The yield stress is a stress value that separates the flow behaviour into two distinctly different qualitative regimes. If the shear stresses in the fluid lie below the yield stress, then the fluid has a solid-like structure and moves as a rigid body. If the shear stresses in the fluid exceed the yield stress, then the fluid deforms as a (nonlinearly) viscous fluid and is typically shear-thinning since the fluid structure breaks down progressively with shear. The most common rheological models of this form are the Bingham, Casson and Herschel–Bulkley fluids.

The key feature of our methodology is best illustrated by considering a steady core–annular flow of iso-density fluids (see figure 1). The shear stress increases linearly from the pipe centre to the outer wall. The main idea is to position the visco-plastic fluid in the outer lubricating layer and ensure that the yield stress ($\hat{\tau}_Y$) is larger than the interfacial shear stress ($\hat{\tau}_i$) by a finite amount. This has the effect of assuring that there is an unyielded solid-like ring of visco-plastic fluid surrounding the core fluid. Indeed since the yield stress exceeds the interfacial stress by a finite amount, we would expect that finite perturbations are needed to yield the fluid at the interface, permitting instabilities to grow. The above idea is simplistic, but has been further developed by Frigaard (2001), Moyers-Gonzalez, Frigaard & Nouar (2004) and Huen, Frigaard & Martinez (2007).

Frigaard (2001) studied the linear stability of a configuration similar to that in figure 1, but in a plane channel geometry and with the inner fluid also a Bingham fluid. Linear stability studies of Bingham fluids date back to Frigaard, Howison & Sobey (1994) who show that the unyielded regions of parallel shear flows are not perturbed by linear perturbations (since the perturbations are modal, the stress perturbations average to zero longitudinally). In Frigaard (2001), the same analysis is applied, resulting in a decoupling of the stability problems for the two fluids. Via a mapping technique, each linear stability problem is then shown to be more stable than the linear stability problem of the same fluid flowing alone in the channel. The approach used by Frigaard *et al.* (1994) and Frigaard (2001) involves considering the even extensions of a linear eigenvalue problem, following a symmetry argument which has been questioned by Nouar *et al.* (2007). The full-domain eigenvalue problem has been extensively studied by Nouar *et al.* (2007) and no unstable modes have been found. Nouar *et al.* (2007) also present a convincing argument for the unconditional linear stability of this flow. In either case, one can say that flows of the type illustrated in figure 1 will not become linearly unstable to interfacial modes.

https://doi.org/10.1017/S0022112010006348 Published online by Cambridge University Press

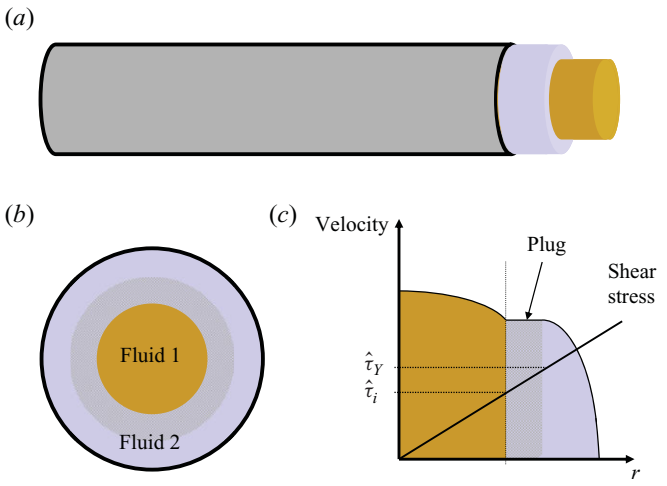


FIGURE 1. (Colour online at http://journals.cambridge.org/FLM) Schematic of the flow geometry: (*a*) axisymmetric core–annular flow; (*b*) cross-section of the pipe; (*c*) velocity and stress profile across a radial section, showing unyielded plug configuration at the interface.

Moyers-Gonzalez *et al.* (2004) explore the nonlinear stability of these flows. The configuration chosen consists of a Bingham lubricating fluid and a Newtonian core, as we also use in this paper. The main method used by Moyers-Gonzalez *et al.* (2004) is the energy stability method, but there are various complications due to the two fluids and possibilities of interfacial motion. For general two-fluid flows, energy stability methods are not particularly useful as the interface topology is unknown and may vary significantly. Moyers-Gonzalez *et al.* (2004) consider only perturbations for which the fluid at the interface remains unyielded in a cylinder about the core fluid, but do not restrict the interface motion. The unyielded cylinder may translate in the axial direction and may translate and rotate within the plane of the cross-section. These restrictions allow the interface motion to be described in terms of the bulk fluid motion and in this way energy decay is established. Although Moyers-Gonzalez *et al.* (2004) show energy decay, they in fact show that the perturbed flow decays only to a base flow that has a Newtonian core encapsulated within the Bingham fluid surrounded by an unyielded ring of fluid, but not necessarily to the concentric base flow. The results of Moyers-Gonzalez *et al.* (2004) are not weakly nonlinear results, but are conditional on the perturbation amplitude. This dependence is not easy to resolve quantitatively (except if the core fluid domain remains concentrically positioned) and this makes the results unwieldy. A second drawback is the usual one of energy stability, namely that the method tells us little about the structure of the actual perturbations as they decay. Finally, the method is also conservative. Thus, the main contribution of Moyers-Gonzalez *et al.* (2004) is in establishing that the flows are nonlinearly stable and hence in some sense robust, without quantifying this robustness. The latter part of our paper is focused at addressing some of this deficiency in understanding.

Huen *et al.* (2007) demonstrate that these flows can be achieved experimentally. They use aqueous Carbopol and Xanthan solutions as the base fluids (Carbopol has a yield stress, Xanthan is shear-thinning). Four sequences of experiments are conducted using different concentration solutions with slightly different rheologies. In each case, stable multi-layer flows are found, where they are predicted to be by the existence of base flows of the type illustrated schematically in figure 1. Unstable flows are

https://doi.org/10.1017/S0022112010006348 Published online by Cambridge University Press

found where these base flow solutions do not exist. In addition, where stable multi-layer flows are found, they appeared to be both stable and concentrically positioned. However, due to practical restrictions on the possible fluid types, on the pump flow rates as well as costs of performing the experiments, the study in Huen *et al.* (2007) was necessarily not a broad systematic study, but rather a proof of concept.

This paper concerns flows such as in figure 1. Overall, our programme of study seeks to establish the practicality of this method for some of the applications discussed above, at least in the fluid mechanic context. Different aspects of this study include the following:

(i) Extension of the flows to different flow scenarios (e.g. new fluid types, different flow geometries) while retaining the basic method of eliminating interfacial instabilities.

(ii) How to establish these flows and how the start-up characteristics of the flow depend on the dimensionless model parameters and inlet geometry.

(iii) Understanding the stability of these flows in greater detail, e.g. what role does the unyielded plug play, do perturbations remain concentric or develop asymmetries, how large an amplitude of perturbation can be withstood and at what Re, etc.

The first of these is being addressed by ongoing studies of using visco-elastic core fluids in place of the Newtonian. We hope to report on these results in the near future. Instead, our study looks at the latter two features: start-up flows and stability, while focusing on the simplest rheological pair (a Bingham lubricating fluid and Newtonian core fluid).

Although the flow that we study is a parallel multi-layer flow shear, the start-up phase of the flow involves filling the pipe with Bingham fluid and then injecting both fluids simultaneously. This flow is more akin to a miscible displacement flow, which has been studied in detail, both experimentally and numerically. In experimental studies, large Péclet number (Pe) is common, e.g. Petitjeans & Maxworthy (1996) study displacements over a range of Péclet, Atwood (At) and Stokes-buoyancy numbers, using a glycerine–water system which only can give Pe in the range $Pe \gtrsim 400$. For the large Pe regime, depending on At (or viscosity ratio m), quasi-steady viscous fingers may form and propagate with a *sharp* displacement front that is retained over $O(1)$ time scales, or longer. A mix of experimental, computational and asymptotic methods have been used to study this regime; the reader is referred to Rakotomalala, Salin & Watzky (1997), Yang & Yortsos (1997), Lajeunesse *et al.* (1997, 1999), Lajeunesse (1999), Scoffoni, Lajeunesse & Homsy (2001), Lajeunesse *et al.* (2001), Kuang, Maxworthy & Petitjeans (2003), Balasubramaniam *et al.* (2005). As $Pe \to \infty$, those displacements that are stable appear to approach the analogous immiscible fluid results, as has been shown experimentally, as well as in a formal asymptotic sense and computationally; see, e.g. Petitjeans & Maxworthy (1996), Chen & Meiburg (1996), Rakotomalala *et al.* (1997), Yang & Yortsos (1997). Considering generalised Newtonian fluids in tubes and between parallel plates, the formal high Pe limit has been considered in the lubrication limit by Bakhtiyarov & Siginer (1996), Allouche, Frigaard & Sona (2000) and Taghavi *et al.* (2009). The propagation of fingers in fully two-dimensional (2D) displacement flows of yield stress fluids is considered both computationally and analytically in Allouche *et al.* (2000) and Frigaard, Scherzer & Sona (2001). Related experimental studies are those of Gabard (2001) and Gabard & Hulin (2003). It is worth mentioning that of the above studies, the vast majority are concerned with finger propagation, efficiency of displacements and residual layers, rather than stability of the flow; see, e.g. Goyal & Meiburg (2006), Goyal, Pichler & Meiburg (2007) and Sahu *et al.* (2009*a*). There is also extensive literature on

https://doi.org/10.1017/S0022112010006348 Published online by Cambridge University Press

immiscible displacements in capillary tubes, including Newtonian and non-Newtonian effects.

Moving now to multi-layer flows, the main focus is on stability of the flow. There are a number of studies of multi-layer flows without a yield stress. These studies are in both planar and axisymmetric geometries, but since the usual instability is interfacial the base flow is less significant than here. For Newtonian fluids perhaps the earliest study of viscosity-stratified shear flow is the classical study of Yih (1967). Later work includes studies of multi-layer Couette, Poiseuille and Couette–Poiseuille flows of Newtonian fluids, e.g. Hickox (1971), Hooper & Boyd (1987) and Yiantsos & Higgins (1988). A fairly extensive review of this literature is given in Joseph & Renardy (1993), which also includes the many contributions of the authors to the study of core–annular flows; see also Joseph *et al.* (1997). Broadly speaking, the linear stability of immiscible iso-density flows requires a sufficiently large surface tension and that the lubricating fluid is less viscous. Surface tension stabilises short-wavelength interfacial modes and the viscosity ratio tends to stabilise long-wavelength instabilities. More recent contributions to this field are by Shariati *et al.* (2004) and Talon *et al.* (2004), who consider a plane channel core–annular flow.

Other than Newtonian fluids, a number of authors have considered the linear stability of multi-layer flows of inelastic non-Newtonian fluids, e.g. power-law fluids are treated extensively in Waters (1983), Waters & Keeley (1987), Khomami (1990) and Su & Khomami (1991). Carreau-Yasuda and (regularised) Bingham-like fluids are treated in Pinarbasi & Liakopoulos (1995). In brief, these results are qualitatively similar to those found for Newtonian fluids, i.e. linear interfacial instabilities arise at small to moderate Reynolds numbers. Importantly, these studies do not consider fluids with a yield stress and unyielded plug at the interface. Explanations of the physical mechanisms that govern this type of instability for Newtonian fluids have been offered by Hinch (1984), Charru (1998) and Charru & Hinch (2000). We believe these explanations can be largely extended to purely viscous generalised Newtonian fluids. In simple terms, sufficiently close to the fluid–fluid interface, the non-Newtonian (nonlinear) character of any purely viscous generalised Newtonian fluid is simply not recognised, i.e. the dominant feature at the interface is a discontinuity in a finite constant viscosity between two fluids.

In the context of miscible multi-fluid flows, there is less work on shear instabilities. In the first place, the term *multi-layer* is ill-defined if the fluids can mix completely. Where linear stability studies have been performed, the parallel base state is assumed quasi-steady. This assumption and the necessity to specify a closure law relating viscosity to fluid concentration lead to inherent difficulties in establishing the generality of results. Ranganathan & Govindarajan (2001) and Govindarajan (2004) analysed the stability of miscible fluids of different viscosities flowing through a channel in a three-layer Poiseuille configuration. They obtained instabilities at high Schmidt numbers and low Reynolds numbers, resembling those of Yih (1967). In Couette flow, it appears that the stability characteristics of the miscible flow are predicted by those of the immiscible flow with zero surface tension; see Ern, Charru & Luchini (2003). However, for core–annular flow, this is not the case; see Selvam *et al.* (2007). It does appear true that introduction of a diffuse layer of intermediate concentration and rheological properties does serve to stabilise the flow. On the other hand, non-monotone variations in rheological properties can lead to shear-type instability, as in the reactive flows studied by Burghelea *et al.* (2007).

More recently, interest has focused on convective instabilities in miscible multi-layer flows. d'Olce (2008) and d'Olce *et al.* (2008) studied experimentally a miscible

https://doi.org/10.1017/S0022112010006348 Published online by Cambridge University Press

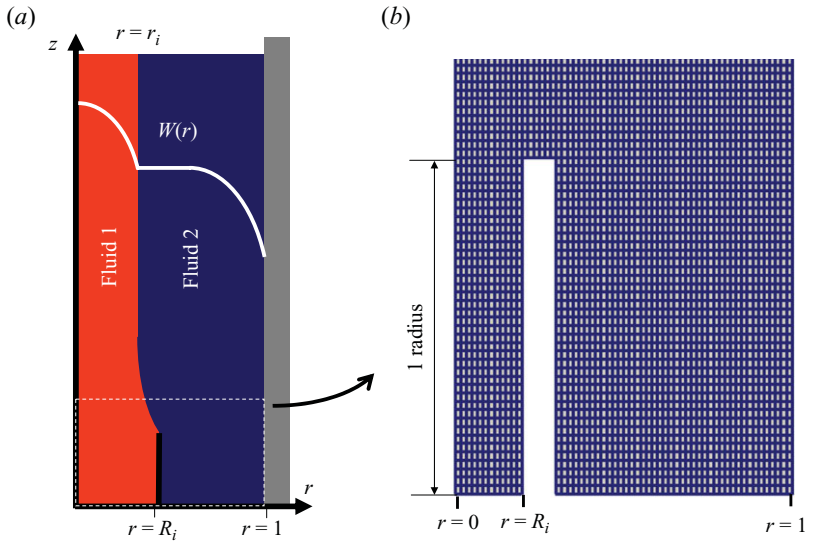


FIGURE 2. (Colour online) (*a*) Schematic of the dimensionless flow geometry in an axisymmetric pipe; (*b*) example computational mesh close to the inlet region for $R_i = 0.2$.

core–annular flow with more viscous fluid adjacent to the wall. On controlling the respective flow rates, one can adjust the equilibrium radius of the interface. As this interfacial position was increased, a number of interesting secondary flows were observed, resembling pearls at smaller interfacial radii and mushrooms at larger radii. A similar transition was effected by increasing Re. This flow has been studied more deeply, both experimentally by d'Olce *et al.* (2009) and computationally/analytically by Selvam *et al.* (2009) in an effort to understand the transition between convective instability and absolute instability. In a related vein, Sahu *et al.* (2009*a*) have recently considered the onset of convective instabilities in three-layer plane channel flows.

An outline of our paper is as follows. Section 2 introduces the physical model of the flows that we study and also outlines the numerical method and various computational studies used to validate the code. Section 3 presents the results of our study of start-up flows and development lengths. Nonlinear temporal stability is studied in § 4 and the paper ends with a brief discussion (§ 5).

2. A multi-layer flow model

As explained in § 1, the aim of our study is to understand start-up, development and stability effects in visco-plastically lubricated flows. An axisymmetric pipe flow is considered throughout the paper. The pipe has outer radius $\hat{R}$ and is initially filled with Bingham fluid (fluid 2). The pipe is vertically oriented and we use axisymmetric cylindrical coordinates with $\hat{z}$ pointing upwards along the pipe axis. For time $\hat{t} > 0$, a Newtonian fluid (fluid 1) is injected upwards through a concentrically positioned inner pipe of radius $\hat{R}_i < \hat{R}$, while at the same time the Bingham fluid is pumped through the annular space surrounding this pipe (see figure 2*a*). The Bingham fluid thus acts as a lubricating layer for the Newtonian core fluid. For the stability studies later (§ 4), we consider an axially periodic section of uniform pipe downstream of the inlet.

https://doi.org/10.1017/S0022112010006348 Published online by Cambridge University Press

Although the setting described is general, we consider flow parameters that correspond approximately to those that we can achieve experimentally in our lab. As a guide, we consider radii $0.005\,\mathrm{m} \lesssim \hat{R} \lesssim 0.1\,\mathrm{m}$, mean velocities $0.001\,\mathrm{m\,s^{-1}} \lesssim \hat{U}_0 \lesssim 1\,\mathrm{m\,s^{-1}}$ and suppose that the fluids consist of miscible aqueous solutions of equal density, $\hat{\rho}$. The choice of a Bingham fluid as the lubricant is a simplification of a typical yield stress rheology (which is often shear-thinning) and the Newtonian core is also primarily for simplicity.

Fluid 1 has Newtonian viscosity $\hat{\mu}^{[1]}$ and fluid 2 is characterised by its yield stress $\hat{\tau}^{[2]}_{yield}$ and plastic viscosity $\hat{\mu}^{[2]}$. The total flow rate along the pipe is $\hat{Q}$, which defines the mean axial velocity: $\hat{U}_0 = \hat{Q}/\pi\hat{R}^2$. The pressure is denoted by $\hat{p}(\hat{\boldsymbol{x}}, \hat{t})$, $\hat{\boldsymbol{u}}(\hat{\boldsymbol{x}}, \hat{t})$ is the velocity, $\hat{\boldsymbol{\tau}}^{[k]}_{ij}$ denotes the deviatoric stress tensor in fluid k and $\hat{g}$ is the gravitational acceleration. We model the change between (pure) fluids 1 and 2 via a scalar concentration C, representing the concentration of fluid 2. The Navier–Stokes equations are made dimensionless with the following scaling:

$$\boldsymbol{x} = \frac{\hat{\boldsymbol{x}}}{\hat{R}}, \quad t = \frac{\hat{t}\hat{U}_0}{\hat{R}}, \quad \boldsymbol{u} = \frac{\hat{\boldsymbol{u}}}{\hat{U}_0}, \quad p = \frac{\hat{p} + \hat{\rho}\hat{g}\hat{z}}{\hat{\rho}\hat{U}_0^2}, \quad \tau_{ij} = \frac{\hat{\tau}_{ij}\hat{R}}{\hat{\mu}^{[2]}\hat{U}_0}. \tag{2.1}$$

The dimensionless model considered in our paper is as follows:

$$\frac{\partial u_i}{\partial t} + u_j\frac{\partial u_i}{\partial x_j} = -\frac{\partial p}{\partial x_i} + \frac{1}{Re}\frac{\partial \tau_{ij}}{\partial x_j}, \tag{2.2}$$

$$\frac{\partial C}{\partial t} + u_j\frac{\partial C}{\partial x_j} = \frac{1}{Pe}\frac{\partial^2 C}{\partial x_j^2}, \tag{2.3}$$

$$0 = \frac{\partial u_i}{\partial x_i}. \tag{2.4}$$

Constitutive laws for the two pure fluids are:

$$\tau^{[1]}_{ij} = m\dot{\gamma}_{ij}, \tag{2.5}$$

$$\dot{\gamma}(\boldsymbol{u}) = 0 \Longleftrightarrow \tau^{[2]}(\boldsymbol{u}) \leqslant B, \tag{2.6}$$

$$\tau^{[2]}_{ij}(\boldsymbol{u}) = \left[1 + \frac{B}{\dot{\gamma}(\boldsymbol{u})}\right]\dot{\gamma}_{ij}(\boldsymbol{u}) \Longleftrightarrow \tau^{[2]}(\boldsymbol{u}) > B, \tag{2.7}$$

where

$$\dot{\gamma}_{ij} = \frac{\partial u_i}{\partial x_j} + \frac{\partial u_j}{\partial x_i}, \tag{2.8}$$

$$\dot{\gamma}(\boldsymbol{u}) = \left[\frac{1}{2}\sum_{i,j=1}^{3}\left[\dot{\gamma}_{ij}(\boldsymbol{u})\right]^2\right]^{1/2}, \qquad \tau^{[2]}(\boldsymbol{u}) = \left[\frac{1}{2}\sum_{i,j=1}^{3}\left[\tau^{[2]}_{ij}(\boldsymbol{u})\right]^2\right]^{1/2}. \tag{2.9}$$

The dimensionless model has three principal dimensionless groups, defined by:

$$m = \frac{\hat{\mu}^{[1]}}{\hat{\mu}^{[2]}}, \qquad Re = \frac{\hat{\rho}\hat{R}\hat{U}_0}{\hat{\mu}^{[2]}}, \qquad B = \frac{\hat{\tau}^{[2]}_{yield}\hat{R}}{\hat{U}_0\hat{\mu}^{[2]}}. \tag{2.10}$$

These are the viscosity ratio, Reynolds number and Bingham number, respectively. The Bingham number denotes the ratio of the yield stress of the fluid to a typical viscous stress of the flow. The Reynolds number has been based on fluid 2 properties. The relevant Reynolds number for fluid 1 is mRe. Note that we also have two geometric groups: $R_i = \hat{R}_i/\hat{R}$, the inlet radius ratio, and r_i which is the radial position

https://doi.org/10.1017/S0022112010006348 Published online by Cambridge University Press

of the interface in a parallel multi-layer flow. This latter is governed by the relative distribution of the total flow rate between the two fluids, as we shall discuss below in § 2.1. A final dimensionless group is the Péclet number, $Pe = \hat{R}\hat{U}_0/\hat{D}_m$, with $\hat{D}_m$ being the molecular diffusivity. Typically, we have $Pe \sim 10^6$–10^{10}, for which values the concentration is effectively advected with the flow. The Péclet number is discussed further in § 2.3.1.

In considering a start-up flow (figure 2*a*), we impose uniform axial velocity and concentrations (0 or 1) at the inlets at the base of the pipe. The mean axial velocity that we impose is determined by solving the problem for *base flow*, which is the parallel flow that we are trying to achieve in the downstream region; see the following § 2.1 No slip conditions are imposed at the solid walls, with no flux for the concentration. Outflow conditions are imposed at the exit of the pipe.

2.1. *Basic flows, $Pe \to \infty$*

In the limit $Pe \to \infty$, we recover a model of two immiscible fluids without surface tension. Following Moyers-Gonzalez *et al.* (2004), there are three distinct types of base velocity profiles, $\boldsymbol{u} = (0, W(r))$, for which a Newtonian core fluid is surrounded by a Bingham fluid. The inner core fluid always assumes a characteristic parabolic velocity profile, but the velocity profile in fluid 2 depends on the fraction of the outer layer that is yielded. The case of primary interest here is that for which the inner core is surrounded by a ring of unyielded fluid. With interface at $r = r_i$ and yield surface position $r = r_y$, these flows have $r_i < r_y < 1$ and velocity profile

$$W(r) = \begin{cases} \dfrac{B}{2r_y}\left[\dfrac{1}{m}\left(r_i^2 - r^2\right) + (1 - r_y)^2\right], & 0 \leqslant r \leqslant r_i, \\ \dfrac{B}{2r_y}(1 - r_y)^2, & r_i < r \leqslant r_y, \\ \dfrac{B}{2r_y}\left[(1 - r_y)^2 - (r - r_y)^2\right], & r_y < r \leqslant 1. \end{cases} \tag{2.11}$$

The yield surface position r_y depends only on r_i, B and m. It is computed from the constraint that the mean velocity, averaged over both inner and outer fluid layers, is equal to 1. After some algebra, $r_y \in (r_i, 1)$ is found as the root of the following quartic equation:

$$0 = (r_y)^4 - 4r_y\left(1 + \frac{3}{B}\right) + 3\left(1 + \frac{r_i^4}{m}\right). \tag{2.12}$$

Following Moyers-Gonzalez *et al.* (2004), this solution is denoted as *case 1* solution. As r_i, B and m are varied, the other two solution types are found: a *case 2* solution, for which the outer fluid is entirely yielded, and a *case 3* solution for which the outer fluid is entirely unyielded and stationary. These solutions are described further in Moyers-Gonzalez *et al.* (2004). It is only the case 1 solutions that allow stable visco-plastically lubricated flows. In the three-dimensional (r_i, B, m)-parameter space, the boundary between case 2 and case 1 solutions is given by:

$$B < \frac{12r_i}{r_i^4\left(\dfrac{3}{m} + 1\right) - 4r_i + 3} \tag{2.13}$$

https://doi.org/10.1017/S0022112010006348 Published online by Cambridge University Press

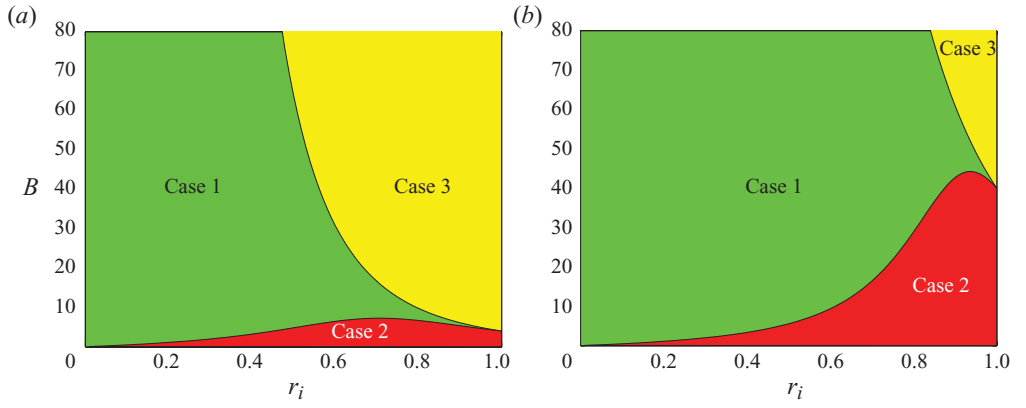


FIGURE 3. (Colour online) Parameter domains where the base solutions are found in (r_i, B, m)-space: (*a*) $m = 1$; (*b*) $m = 10$.

(with case 1 solutions found when this inequality is not satisfied). The boundary between case 3 and case 1 solutions is given by:

$$B > \frac{4m}{r_i^4} \tag{2.14}$$

(again case 1 solutions are found when this inequality is not satisfied). Figure 3 illustrates the domain in which case 1 solutions are found for two different viscosity ratios, m.

Returning to the dimensional parameters of the problem, we recall that for a typical hydraulic flow one can specify either the flow rate or the pressure drop, but not both. The analogy for the multi-layer flows studied is that if one specifies the flow rates of the individual fluid phases, then it can be shown that the pressure drop and the radial interface position are uniquely determined. Conversely (and perhaps more obviously), specifying the pressure drop and radial interface position uniquely determines (the velocity and) the flow rates in the individual fluid phases.

2.2. *Computational solution*

The model equations (2.2)–(2.9) have been discretised using a mixed finite-element/finite-volume method. The Navier–Stokes equations are solved using the Galerkin finite-element method. The computations are carried out on a structured rectangular mesh, with linear elements (Q1) for the velocity and constant elements (P0) for the pressure discretisation. The divergence-free condition is enforced by an augmented Lagrangian technique; see Glowinski & Le Tallec (1989). Although we could use a higher order discretisation, we have not done so. We are cautious about imposing more regularity on the discrete solution than may exist for the solution to the exact Bingham fluid model. A potential disadvantage of our choice of elements is that the inf-sup condition is generally not satisfied by this discretisation. Velocity errors are usually independent of the discrete inf-sup condition; see Brezzi & Fortin (1991). The augmented Lagrangian approach for the divergence-free condition induces L2-stability (dependent on the penalty parameter) for the pressure, making the discretisation less sensitive to effects of spurious pressure modes. We have not observed any evidence of spurious modes or numerical instability in any of our computations. These aspects are discussed in more detail in Brezzi & Fortin (1991) and Quarteroni & Valli (2008).

https://doi.org/10.1017/S0022112010006348 Published online by Cambridge University Press

There are two sources of nonlinearity in the Navier–Stokes equations: the convective terms and the shear stress terms (in the case of the Bingham fluid). Regarding the Bingham fluid, note that the effective viscosity becomes infinite in unyielded regions of the flow, although stress and strain rate tensors remain finite. Two methods are popular for dealing with this. Either one regularises the effective viscosity functional to remove the singular behaviour; see, e.g. Bercovier & Engleman (1980), Glowinski (1983), Papanastasiou (1987) and Frigaard & Nouar (2005). This system can then be solved iteratively as a flow problem with a nonlinear viscosity. Alternatively, one solves the equations using a relaxation-multiplier approach such as the augmented Lagrangian method; e.g. Glowinski, Lions & Tremolieres (1976), Glowinski (1983) and Glowinski & Le Tallec (1989). The regularisation approach replaces the unyielded region with a region of small strain rate and high viscosity. The augmented Lagrangian method gives zero strain rate in such regions. We implemented both strategies in the code development stage. As regularisation method, we have followed Bercovier & Engleman (1980), replacing (2.6) and (2.7) with

$$\tau_{ij}^{[2]}(\boldsymbol{u}) = \left[1 + \frac{B}{[\dot{\gamma}^2(\boldsymbol{u}) + \epsilon^2]^{1/2}}\right] \dot{\gamma}_{ij}(\boldsymbol{u}), \tag{2.15}$$

where we take the regularisation parameter $\epsilon = 10^{-4}$ (see below). Except in cases when the unyielded plug is very thin, we see only minor differences in our results between methods. For this particular flow, it seems that the numerical limit on the unyielded plug thickness is more related to the mesh resolution than to the method used to resolve the stress. The regularisation method gives faster computations than the augmented Lagrangian method (if one discounts the time spent in establishing an acceptable ϵ), and this has been the main reason for our usage. All results presented use this method.

We use a fixed time step for the Navier–Stokes equations, advancing from time step N to $N+1$. Typically, we have $\mathrm{d}t = 0.01$, but for some simulations we have re-computed with a finer time step when a particular flow feature warrants investigation of shorter time scales (e.g. see figure 15). Regarding the implementation of the nonlinear terms, we use a semi-implicit method. The convective velocity is approximated at time step N while the linear spatial derivatives of the velocity are approximated implicitly at time step $N+1$. The effective viscosity is approximated at time step N^* with the strain rate components at step $N+1$. A Picard iteration is then used within each time step to successively update the variables at step N^*, so that the shear stress discretisation becomes successively closer to being fully implicit. The pressure is approximated at time step $N+1$.

The concentration equation (2.3) uses a finite-volume method, in which the concentration is approximated at the centre of each regular mesh cell. The advective terms are dealt with via a Monotone Upstream-centred Scheme for Conservation Laws (MUSCL). These are essentially slope-limiter methods for reducing oscillations close to discontinuities; see e.g. Wesseling (2001) and LeVeque (2002) for more description. On each (Navier–Stokes) time step, a splitting method is used to advance the concentration equation over a number of smaller sub-timesteps. This time advance is explicit and a CFL (Courant–Friedrichs–Lewy) condition is implemented for the sub-timesteps to ensure numerical stability.

The numerical algorithm is implemented in C++ as an application of PELICANS. PELICANS is an object-oriented platform developed at IRSN, France, to provide a general framework of software components for the implementation of

https://doi.org/10.1017/S0022112010006348 Published online by Cambridge University Press

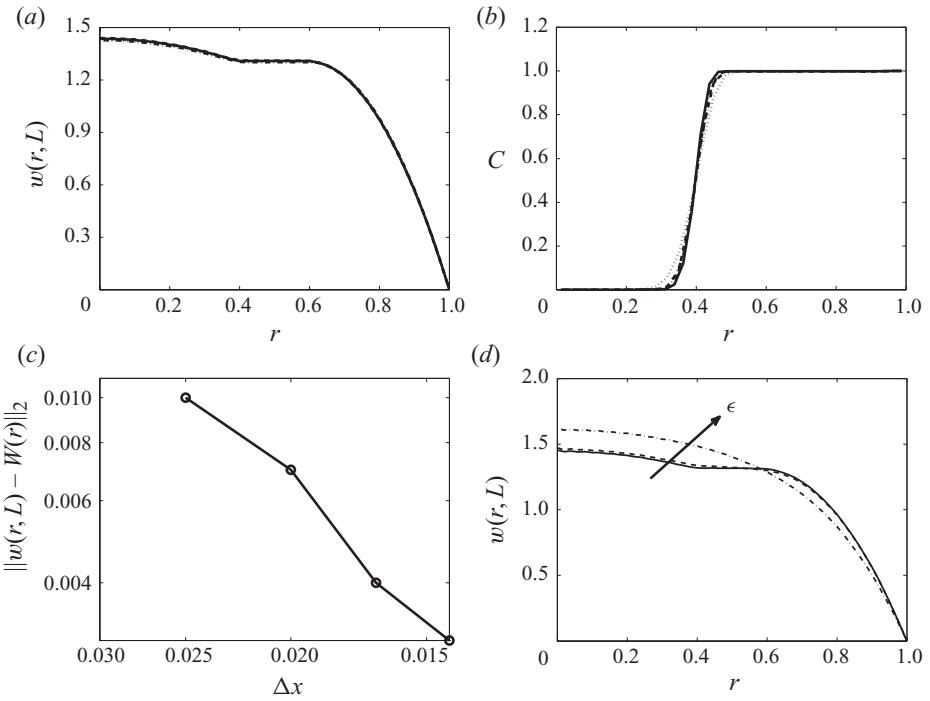


FIGURE 4. Effect of mesh size on: (*a*) exit velocity profile; (*b*) exit concentration profile; (*c*) L^2 norm of difference between exit velocity W and analytic velocity W_a. Flow parameters are: $m = 10$, $Re = 5$, $B = 10$, $r_i = 0.4$ and $R_i = 0.2$. In each plot, line styles (:), (–.), (––) and (–) correspond to $\Delta r = 0.025$, $\Delta r = 0.02$, $\Delta r = 0.017$ and $\Delta r = 0.014$, respectively; Δr is the radial mesh size. (*d*) Effect of regularisation parameter ϵ on computed exit velocity profile W: $\epsilon = 1,\ 0.1,\ 0.0001$.

partial differential equation solvers. PELICANS is distributed under the CeCILL license agreement (http://www.cecill.info/licences/Licence_CeCILL_V2-en.html). PELICANS can be downloaded from https://gforge.irsn.fr/gf/project/pelicans/. Although the equations could have been implemented in a commercial CFD code, these codes are often over-stabilised and give little access to the detailed implementation. We used 60 elements across the pipe and 40 elements per unit along the pipe, which is of dimensionless length L. The length is adjusted according to the physical situation we model and for longer geometries we preserve the mesh density. The inflow section of a typical mesh is shown in figure 2(*b*). Figure 4(*a–c*) shows the difference between the analytic solution and the computed solution at the exit, for various mesh sizes and fairly typical parameters. It can be seen that the velocity is well represented at this mesh resolution and the concentration field also, except at the interface where the jump in concentration is smeared over a few cells. Refinement does reduce the thickness of the diffuse layer, but this effect of numerical diffusion is always present.

For the same parameters as figure 4(*a–c*), we show in figure 4(*d*) and in figure 5 the effects of varying the regularisation parameter ϵ. For $\epsilon = 1$, this is effectively just a shear-thinning fluid, but we observe that even for $\epsilon = 0.1$ the exit velocity and strain rate profiles are converging. Our choice of $\epsilon = 0.0001$ is similar to that made by other authors.

https://doi.org/10.1017/S0022112010006348 Published online by Cambridge University Press

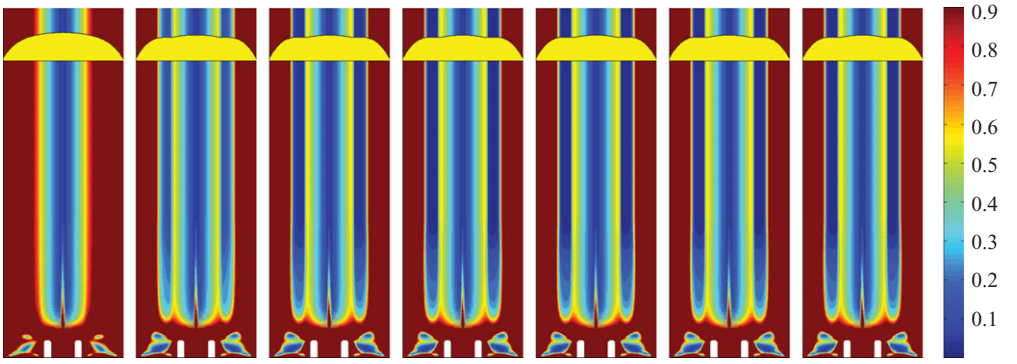


FIGURE 5. Effects of regularization parameter ϵ on computed strain rate: $\epsilon = 1,\ 0.1,\ 0.01,\ 0.001,\ 0.0001,\ 0.00001,\ 0.00001$ (left to right). Flow parameters are: $m = 10$, $Re = 5$, $B = 10$, $r_i = 0.4$ and $R_i = 0.2$.

It is worth commenting that we have not observed any physically spurious instabilities while using the regularisation method. In hydrodynamic stability studies, these instabilities can arise firstly at the interface (which formally is simply *very viscous*), and secondly close to the yield surface where a discontinuity in the second derivative of the velocity is smoothed; see Frigaard & Nouar (2005). Although such instabilities are theoretically possible, they occur in parts of the flow that are *very viscous* (of order B/ϵ) and hence grow very slowly. Thus, even if these additional modes were present in our computations, they would probably not be observable on the time scale of our computations.

2.3. *Code validation*

In order to validate the code implementation, a number of steps have been taken. Firstly, various 1D single-fluid benchmark flows were computed, e.g. pipe and plane Poiseuille flow. Secondly, for the start-up/development flow simulations, we are able to compute analytically the fully developed base flow (as described in § 2.1) which can be compared with the velocity profile at the exit. An example of such a comparison is shown in figure 6. For the range of r_i selected, some of the base flows are of case 1, whereas others are cases 2 and 3. In general, we observe that the comparison between the analytical base flow and computed exit profiles is reasonable. However, as we shall see later, there is a small amount of numerical diffusion/dispersion at the interface which leads to some error. For the computations of figure 6, we have selected $R_i = 0.2$, so that the core fluid expands radially outwards as the developed flow is attained. We shall see later that such flows tend to have the most significant numerical diffusion/dispersion, so effectively we are presenting a worst case scenario. The diffuse interfacial region is also larger when there is strong shear at the interface.

2.3.1. *Diffusive effects*

In view of the large Péclet numbers, we may expect that physical (molecular) diffusion is not significant for the flows we consider. Mixing due to molecular effects only becomes significant on the radial length scale for long pipes, defined in the dimensionless parameters by $L \sim Pe$, which is the Taylor dispersion regime. Here, we are restricted to more practical lengths, $L \lesssim O(10^2)$, and since $L \ll Pe$ we eliminate the diffusive terms from the concentration equation (2.3), by setting $Pe = \infty$ later in the paper.

https://doi.org/10.1017/S0022112010006348 Published online by Cambridge University Press

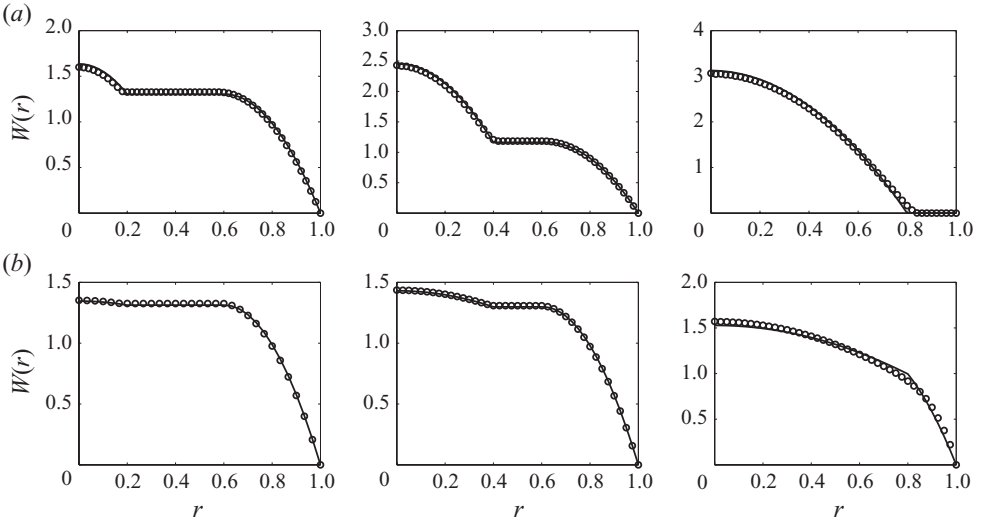


FIGURE 6. Comparison of computed exit axial velocities with the analytic base flow $W(r)$ for $R_i = 0.2$, $Re = 5$, $B = 10$: (*a*) $m = 1$ and from left to right, $r_i = 0.2,\ 0.4,\ 0.8$; (*b*) $m = 10$ and from left to right, $r_i = 0.2,\ 0.4,\ 0.8$. In each plot, the solid line shows the analytic solution and the circle symbols indicate the computed exit axial velocity.

Although we may eliminate molecular diffusion easily, numerical diffusion still remains. These effects are reduced by methods such as a MUSCL scheme, but are not eliminated. As a practical matter, this means that intermediate concentrations $C \in (0, 1)$, are computed during solution of (2.3) in interfacial regions. For such concentrations, we interpolate the constitutive laws of the two fluids, resulting in:

$$\tau_{ij} = \left([C + m(1 - C)] + \frac{BC}{\dot{\gamma}} \right) \dot{\gamma}_{ij} \quad \Longleftrightarrow \tau > BC, \tag{2.16}$$

$$\dot{\gamma}_{ij} = 0, \quad \Longleftrightarrow \tau \leqslant BC, \tag{2.17}$$

and use the pure fluid rheologies for concentrations outside of (0, 1).

To quantify the effects of numerical diffusion in our code, we have performed a sequence of studies at increasing $Pe = 10^2,\ 10^3, \ldots, 10^7$. We fix $R_i = 0.2$, $r_i = 0.4$, $Re = 40$, $B = 10$ and examine the exit velocity and concentration profiles for a channel of length $L = 50$. The results are shown in figure 7. The base flow for these parameters is a case 1 flow with a significant plug region.

The smallest value of Pe ($Pe = 10^2$) is of the same order as L and Re. For this value, molecular and viscous diffusion are equally significant and the length of pipe is sufficient to allow significant diffusive mixing. We observe that over the length of the pipe the two fluids mix completely (see figure 7*b*), giving a mean concentration $\bar{C} \approx 0.7$. Note that the mixture has a Bingham number equal to $B\bar{C}$ and therefore an unyielded plug region is found in the centre of the pipe (see figure 7*a*).

As Pe is increased, the degree of mixing decreases and the interfacial layer becomes progressively less diffuse. For $Pe \geqslant 10^5$, we find that the profiles are indistinguishable from one another. The diffusion is now dominated by numerical effects and unaffected by Pe. The diffuse region occupies a thickness that is determined by the mesh discretisation, corresponding roughly to two to three cells. To give a quantitative

https://doi.org/10.1017/S0022112010006348 Published online by Cambridge University Press

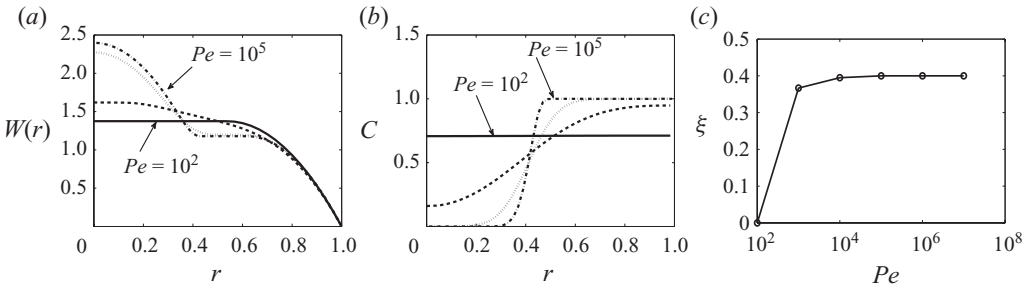


FIGURE 7. Effects of Péclet number on: (*a*) exit velocity profile; (*b*) exit concentration profile; (*c*) numerically defined interface radius ξ. Flow parameters are: $m=1$, $Re=40$, $B=10$, $r_i=0.4$ and $R_i=0.2$.

measure of the interface radius, we define

$$f(C)=\begin{cases}0, & \text{if} \quad C>\frac{1}{2},\\ 1, & \text{if} \quad C\leqslant\frac{1}{2},\end{cases} \tag{2.18}$$

and then integrate to find a numerically defined interface radius, ξ:

$$\xi=\int f(C)\,\mathrm{d}x. \tag{2.19}$$

Figure 7(*c*) shows the variation of ξ with Pe, converging approximately to $r_i=0.4$. The numerical interface position is evidently sensitive to mesh refinement, even as $Pe\to\infty$. Although we could further refine our mesh to reduce numerical effects and perhaps then include physical diffusion via a finite Péclet number, a mesh size of order $Pe^{-1/2}$ would be required and this quickly becomes prohibitive in terms of computational times required, especially for larger Pe ranges.

Although the interpolation of (2.16) and (2.17) is simplistic and imposing $Pe=\infty$ is also partly for simplicity, it is worth noting that providing a more physically realistic model is not easy. In modelling miscible Newtonian flows, polynomial splines, exponential and power-law interpolations have all been used as different examples of viscosity closure laws: e.g. Sahu *et al.* (2009*a*), Selvam *et al.* (2007) and Yang & Yortsos (1997), but there is evidently no universal closure. All that can be done to establish the robustness of results is to benchmark different closure models over a reasonable range of flows. In preliminary computations, we have tested the exponential interpolation of Selvam *et al.* (2007) and the power-law interpolation of Yang & Yortsos (1997), finding little noticeable difference in results. Secondly, if we were to model the molecular diffusivity, it would not be constant in the yield stress fluid. Indeed, if we accept the idealisation of the Bingham model as a rigid solid when unyielded, then the molecular diffusivity will certainly be drastically reduced in these regions (according to the specifics of the gel structure) so that $Pe=\infty$ may not be a poor approximation.

2.3.2. *Pearls and mushrooms*

While comparisons such as figure 6 illustrate that our code is able to simulate the development of stable established base flows, in the second part of this paper, we wish to study evolution of transient-imposed perturbations. In order to demonstrate that more complex transient flow structures can also be simulated, we have conducted a number of comparative computations in order to simulate the recent experimental

https://doi.org/10.1017/S0022112010006348 Published online by Cambridge University Press

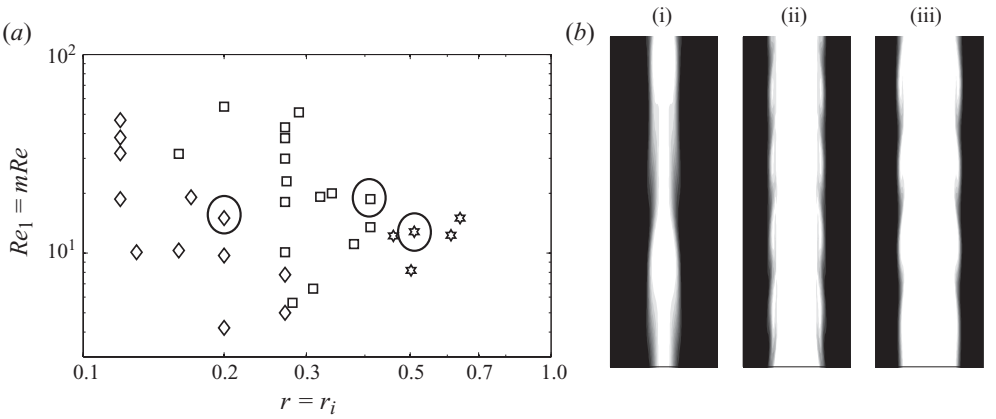


FIGURE 8. Pearl and mushroom patterns computed in $(Re_1, r) = (mRe, r_i)$ space. In (a) ★ indicates observed mushroom-like flows without any flow perturbation; ◇ and □ indicate pearl-like and mushroom-like flows, respectively, observed with a small flow perturbation. (b) The plots illustrate the flow parameters circled (left to right): (i) pearl-like pattern for $r_i = 0.2$, $Re_1 = 15$; (ii) mushroom-like pattern for $r_i = 0.411$, $Re_1 = 18.7$; (iii) mushroom-like pattern for $r_i = 0.51$, $Re_1 = 12.8$.

results of d'Olce (2008) and d'Olce *et al.* (2008). In these experiments, two iso-density miscible Newtonian fluids with different viscosities were pumped concentrically into a pipe. The ratio of outer to inner fluid viscosity was 25 and a range of different relative flow rates were tested, producing beautiful 'pearl' and 'mushroom' shaped patterns.

In the context of our model problem, we have $m = 25$, $B = 0$ and a range of different r_i, according to the different relative flow rates. Since there is no yield stress, all base flows are case 3, but equally since there is no unyielded plug, the interface can deform and mix. The experimental regime studied by d'Olce (2008) and d'Olce *et al.* (2008) considers relatively moderate Re and the authors estimate their Péclet number in the range 2×10^4–6×10^5, so that although the fluids are miscible, purely diffusive effects are minimal. In figures 8 and 9, we present our numerical simulation results for a wide range of the parameters explored experimentally in d'Olce *et al.* (2008). For these figures only, the Reynolds number Re_1 is the fluid 1 Reynolds number, as used by d'Olce and co-investigators (i.e. mRe in terms of our parameters). The parameter r in d'Olce *et al.* (2008) is equivalent to r_i used here.

The first observation, in comparison with d'Olce *et al.* (2008) is that we are able to get qualitatively and quantitatively similar instability patterns using our numerical code. We note that quantitative comparisons beyond comparing the radial perturbations of the diffusive interface are difficult: the figures presented in d'Olce *et al.* (2008) are images (from which a *concentration* might be inferred), whereas the results shown here represent a quantitatively computed concentration, displayed in greyscale for comparison purposes. Nevertheless, it is clear that our numerical simulation can capture the same flow features as those observed experimentally in representative multi-layer flows.

Figure 8(a) illustrates where pearl and mushroom patterns have been computed in (Re_1, r_i) space (compare with figure 6 in d'Olce *et al.* 2008). Mushroom-like patterns can be found with no flow perturbation for $r_i > 0.45$, but for small $r_i \lesssim 0.45$ we found it necessary to slightly perturb the flow at the inlet, for both pearl-like and mushroom-like patterns. We impose base constant flow rates Q_1 and Q_2, in fluids 1

https://doi.org/10.1017/S0022112010006348 Published online by Cambridge University Press

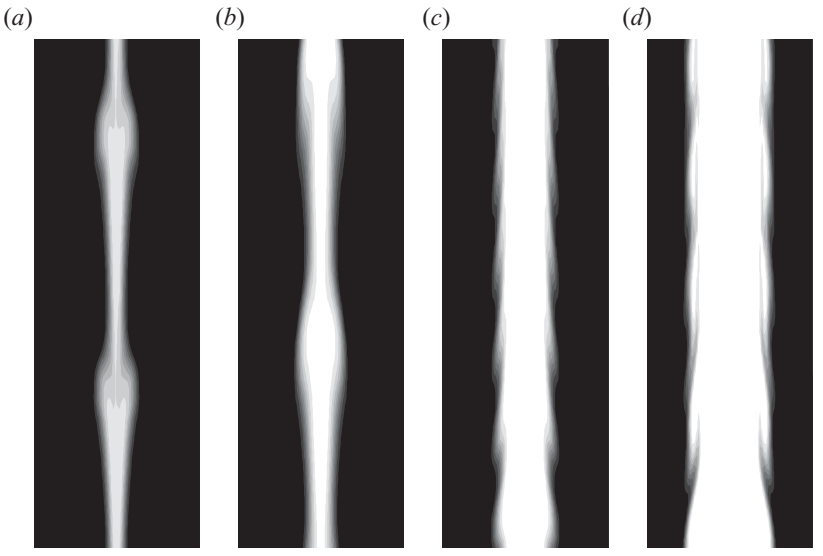


FIGURE 9. Illustration of the pearl to mushroom transition as r_i is increased, for $Re_1 = 19$: (*a*) $r_i = 0.12$; (*b*) $r_i = 0.17$; (*c*) $r_i = 0.27$; (*d*) $r_i = 0.411$.

and 2, respectively, with $Q_1 + Q_2 = 1$. We then slightly perturb these flow rates as follows:

$$Q_1 \to Q_1 + \delta \sin 2\pi f t, \qquad Q_2 \to Q_2 - \delta \sin 2\pi f t. \tag{2.20}$$

For the frequency f, we choose $f = u_i/\lambda$, where u_i is the interface velocity of the base flow and λ is the wavelength of perturbation observed in d'Olce *et al.* (2008). Typically, we have been able to excite the patterns observed for $r_i \lesssim 0.45$ by using amplitudes $\delta < 5\,\%$ (and in all cases $\delta < 10\,\%$).

It is interesting to observe that our simulations are computed with $Pe = \infty$ in (2.3), whereas the study in § 2.3.1 indicates that numerical effects dominate for $Pe \gtrsim 10^5$. Although for at least a good part of the computed results our (numerical) diffusive effects are smaller than molecular diffusive effects (as reported in the experimental work), we find in fact quite similar diffuse patterns. This highlights the strong role of dispersive secondary currents in such flows. Although the diffusion we calculate is non-physical, the observed dispersive effects are predominantly physical.

3. Start-up and entry length effects

Two aspects of the initial part of the core–annular flow are of interest. Firstly, is it possible to establish the base multi-layer flows at all, i.e. from a practically realisable initial flow configuration? If realisable, how robust is this initial flow? Secondly, having established a base flow, what factors affect the entry or development length of the flow? Whilst the latter problem could be studied via a steady flow computation, we have in fact studied both questions via a transient flow computation.

As an initial condition, the entire pipe is filled with pure fluid 2. For fixed (m, B), the parameter r_i defines the relative flow rates Q_1 and Q_2 in each phase, such that $Q_1 + Q_2 = 1$. The individual flow rates are translated into constant mean inflow velocities, which are applied at the inlets of the inner pipe and annulus for $t > 0$. Also, for $t > 0$, we impose $C = 0$ at the inflow of the inner pipe, with $C = 1$ imposed

https://doi.org/10.1017/S0022112010006348 Published online by Cambridge University Press

at the annulus inflow. The computations are run until the inner fluid exits the pipe at $z = L$ and the flow becomes steady. The final steady flow is used for our calculations of entry (or development) length.

3.1. *Start-up flows*

Typical examples of the start-up phase of the flow are shown in figures 10 and 11. In figure 10, we show some of the effects of the ratio r_i/R_i. In each row, the first three plots show C at times $t = 4,\ 8,\ 12$. In each case, we observe that the initial front of fluid 1, penetrating into fluid 2 is destabilised locally, with a recirculating vortex developing at the sides. The extent of this feature varies with r_i/R_i, but does not destabilise the flow behind the front. The recirculation leads to significant dispersive mixing between the fluids in this region. Beyond $t = 12$, this recirculating pattern simply is advected up the pipe and out the exit, leaving behind the smooth multi-layer configuration. Looking between the first three frames, we see that the frontal region does grow as it propagates, and hence should be termed convectively unstable, but is not absolutely unstable.

The following three plots on each row of figure 10 show further features of the flow at $t = 12$. From right to left, they show the speed, the absolute value of the shear stress and strain rate, respectively. On the shear stress plot, we contour explicitly $\tau = B$, denoting the yield surface when in fluid 2. On the strain rate plot, we have superimposed the axial component of velocity at three different heights. The plug-like velocity profile is evident in fluid 2, ahead of the front, in both speed and stress plots. The parameters $B = 10$, $r_i = 0.4$, $m = 1$, have a case 1 base solution, see figure 3(a). On the right-hand figure, we observe that this base flow profile is established in the axial flow region behind the front. Formation of the plug region around the core fluid appears to take longer for the expansion inflow (figure 10b) and we note that this is also the flow which has the most significant dispersive mixing at the front. Having said this, it is clear that the base flow is established in each case.

Figure 11 explores the effects of varying viscosity ratio m with all other parameters fixed. The results for $m = 1$ are shown in figure 10(b) and can be compared with those for $m = 10$ and $m = 0.1$ in figure 11. Note that m is the ratio of inner/outer fluid viscosity. For small m, the core fluid moves much faster ahead of the outer fluid. This leads to a large change in velocity gradient across the interfacial region. In contrast, for a case 1 solution with large m, across the interface we have a transition from zero strain rate in the plug to strain rate of $O(1/m)$ in the core fluid. We can see the effects of this change by comparing figures 11(a) and 11(b).

Note first that $L = 60$ in figure 11(a) ($m = 0.1$), so the aspect ratio in figures 11(a) and 11(b) is different. For $m = 0.1$, the large change in shear rate across the interfacial region leads to strong dispersive mixing. Although there is in fact a case 1 base solution for $m = 0.1$, most of the flow rate is focused in the core fluid. Dispersive mixing means that in the mixed region part of the mixture is fluid 2. The result is a very slowly moving plug with narrow yielded layer at the wall. In the near-axial region behind the front, there is a smooth transition in C and also in the strain rate, all due to mixing. If we examine the yield surface structure close to the inlet geometry, we can see that fluid 2 is unyielded in a plug attached to the wall, just ahead of where the inlet pipe ends. We can see a relatively high velocity jet-like region, shaped by the yield surface. This jet focuses fluid 2 inwards towards the core and enhances mixing. Further up in the pipe we have recirculatory motion about the displacement front and further mixing. The two effects combine to give the long dispersive 'tails' evident in the $t = 12$ concentration plot, extending down towards the inlet. As there are both inlet effects

https://doi.org/10.1017/S0022112010006348 Published online by Cambridge University Press

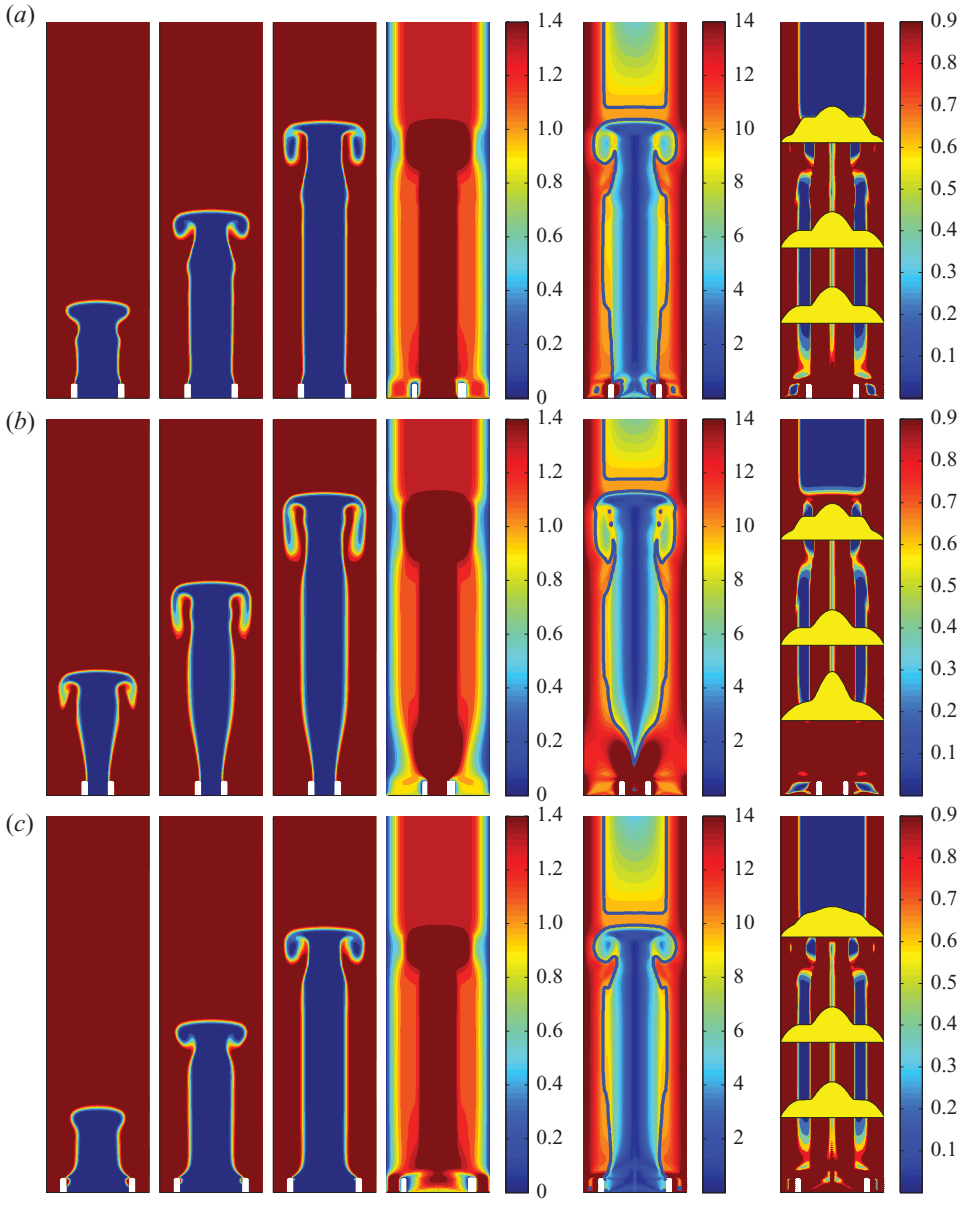


FIGURE 10. Start-up flow for $B=10$, $r_i=0.4$, $m=1$, $Re=20$, $L=25$: (*a*) $R_i=0.4$; (*b*) expansion, $R_i=0.2$; (*c*) contraction, $R_i=0.6$. In (*a*)–(*c*), the first three plots show C at times $t=4$, $t=8$ and $t=12$, respectively. The fourth plot is a colourmap of the speed at $t=12$. The fifth plot shows the shear stress at $t=12$, with value $\tau=B$ highlighted. The sixth plot shows the strain rate $\dot{\gamma}$ at $t=12$. On this figure we have superimposed the computed axial velocity profiles at selected distances along the pipe.

and dispersion backwards from the front, it is unclear how to categorize this flow, except as convectively unstable. At later times, the frontal region does advect from the pipe, leaving behind a parallel unyielded interface, but the mixing induced by the jetting in the inlet region does not cease.

https://doi.org/10.1017/S0022112010006348 Published online by Cambridge University Press

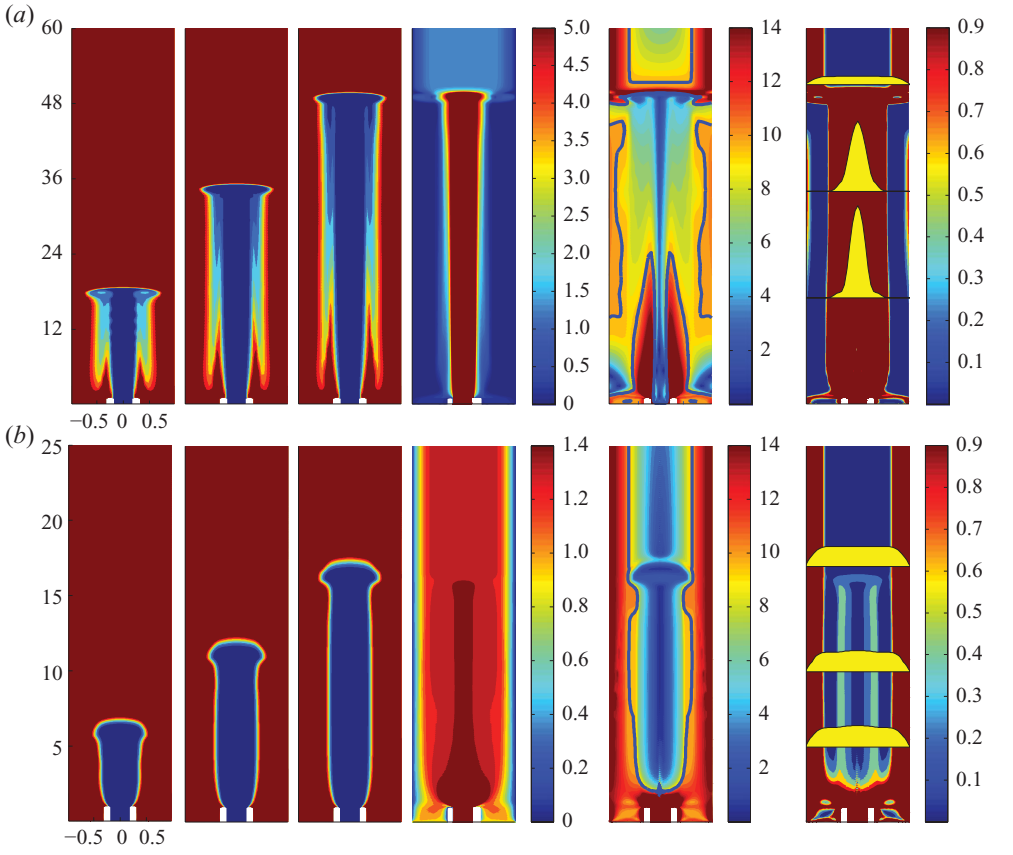


FIGURE 11. Start-up flow for $B = 10$, $r_i = 0.4$, $Re = 20$, $R_i = 0.2$: (*a*) $m = 0.1$, $L = 60$; (*b*) $m = 10$, $L = 25$. See caption of figure 10 for description of the different plots.

The flow for $m = 10$ is quite different. By comparing with $m = 1$ (figure 10*b*), we observe that the larger viscosity in the core fluid acts to suppress the recirculation and instability at the front, evident in figure 10(*b*). We appear to approach the base flow very quickly and there is minimal dispersive mixing anywhere in the flow.

The results shown are typical in that the frontal dispersive region is eventually advected from the pipe, replaced by the near-parallel flow. We have not explored a large variation in B, since at fixed m and r_i as we vary B we transition from case 2 to case 1 to case 3 base flows, whereas our interest is exclusively the case 1 flows. Similarly, we have some computational restrictions in Re. The development length grows with Re, necessitating increasingly long domains for $R_i \neq r_i$. At the same time, we wish to retain the mesh resolution in the axial direction in order to resolve dispersive effects at the front and elsewhere. This results in a very expensive computation that becomes infeasible for pipe aspect ratios $L > 100$. For geometries $R_i = r_i$, entry lengths are markedly reduced and we have been able to compute start-up flows for Re in the range 100–500, but have not studied this regime systematically.

It is worth noting at this stage that we have not found parameters for which a stable steady configuration was not achieved for a case 1 base flow parameter set. This suggests that for $Re < 50$, although the initial frontal displacement is convectively unstable the axisymmetric flow produced is temporally stable and appears to be robust

https://doi.org/10.1017/S0022112010006348 Published online by Cambridge University Press

over a range of different inlet/outlet radius ratios. The method of starting the flow is identical with that used experimentally in Huen *et al.* (2007), but is certainly not the only method possible.

3.2. *Development lengths*

Process design requires some estimate of the length of pipe required for the flow to develop, and how this length varies with the principal parameters. We take these estimates from the final computed time of the start-up computations, described above.

An example of the final computed flows is shown in figure 12. Each row shows results for $r_i = R_i$ as well as for a typical expansion and contraction (at the same fixed r_i, so that the final base flow is identical). From (*a*) to (*c*), the Reynolds number is increased. In each simulation, we show C at the final time and also the magnitude of the rate of strain. For all figures shown, the final base state is identical.

Two features are evident from figure 12. Firstly, the flow develops more quickly with the inlet radius closer to the established interface radius r_i. Secondly, we can see that increasing Re retards development of the base flow. Less obvious is that the thickness of the diffuse interfacial layer increases slightly with Re and for $R_i \neq r_i$. Essentially, the longer the development length is the more time there is for numerical diffusion and dispersion to occur.

Careful examination of results such as those in figure 12 reveals that there are in fact different interpretations of the flow development possible. In the first place, as case 1 solutions require an unyielded plug region surrounding the core fluid, it is of interest to know the first point at which this unyielded plug begins to form. We characterise this by L_τ, defined as the distance from the inlet at which the first unyielded fluid is found.

A second entry length consideration in a multi-layer flow is whether the interface becomes parallel and approaches the established radius. As we have seen, a diffuse region emerges around the interface and this makes direct comparison with the analytical r_i problematic as a means of defining flow establishment. For example, the exit flows for contraction and expansion are no less established than those for $r_i = R_i$. It is simply that the thickness of the diffuse interfacial layer is larger. Therefore, we have used the following definition to denote where the concentration field is established. We define L_c as the smallest z that satisfies the following inequality:

$$\frac{(L - L_c)}{\|C\|_{2r}(L)} \left\| \frac{\partial C}{\partial z} \right\|_{2r}(z) \leqslant 0.01, \tag{3.1}$$

where for a function $f(r, z)$, we define $\|f\|_{2r}(z)$ by:

$$\|f\|_{2r}(z) = \left[\int_0^1 r|f(r, z)|^2 \, \mathrm{d}r \right]^{1/2}. \tag{3.2}$$

In addition, we verify that the diffuse interfacial layer is centred on $r = r_i$.

Finally, we wish to define an entry length for the velocity, say $z = L_u$. We have similar problems in this definition in comparing against the analytical solution, due to diffusive effects. Therefore, we again define L_u as the smallest z that satisfies the following inequality:

$$\frac{(L - L_u)}{\|W\|_{2r}} \left\| \frac{\partial w}{\partial z} \right\|_{2r}(z) \leqslant 0.01, \tag{3.3}$$

where $W = W(r)$ denotes the analytic velocity profile given by (2.11) and $w(r, z)$ is the computed z-component of velocity.

https://doi.org/10.1017/S0022112010006348 Published online by Cambridge University Press

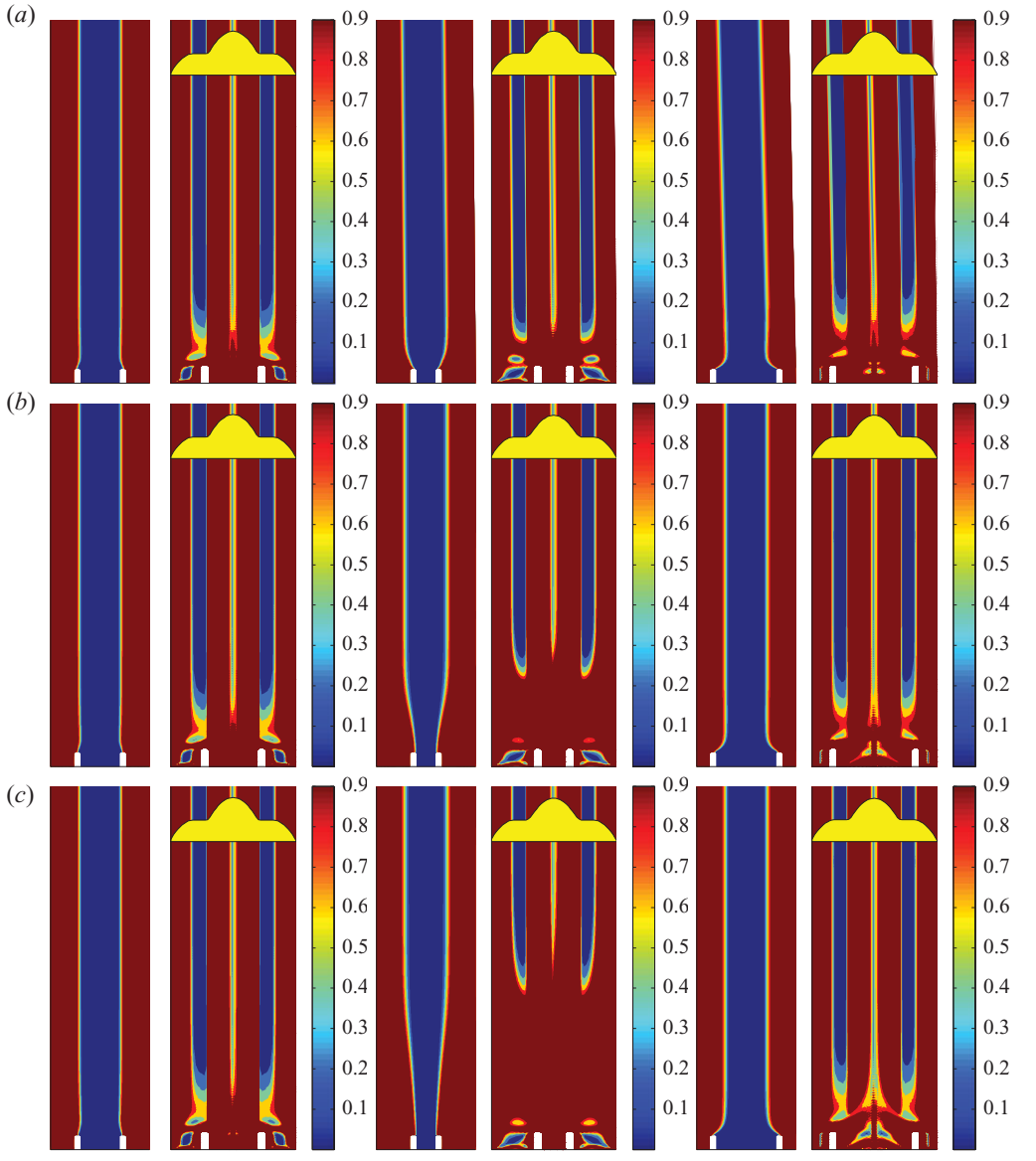


FIGURE 12. Steady developed flow for $m=1$, $B=10$: (*a*) $Re=5$; (*b*) $Re=20$; (*c*) $Re=40$. Each row shows (left to right): $R_i=r_i=0.4$; $0.2=R_i<r_i=0.4$; $0.6=R_i>r_i=0.4$. For each parameter set, we show C and $\dot{\gamma}$, with the computed axial component of velocity superimposed near the outflow.

Figure 13 shows the different development lengths and how they vary as the ratio r_i/R_i is changed along with m, Re and B. In each row, we present the different entry lengths L_τ, L_c and L_u, respectively. Each figure consists of data from two sets of simulations at fixed R_i: firstly, $R_i=0.6$ with $r_i=0.2,\ 0.4,\ 0.6$ (contraction flows), and secondly $R_i=0.2$ with $r_i=0.2,\ 0.3,\ 0.4,\ 0.5$ (expansion flows). In each row, we vary either m, Re or B. In all cases, we verify that there exists a case 1 base flow.

The overall trends are as follows. In all cases, we have an ascending hierarchy of development lengths: $L_\tau<L_c<L_u$. The minimal entry lengths are found at $r_i=R_i$,

https://doi.org/10.1017/S0022112010006348 Published online by Cambridge University Press

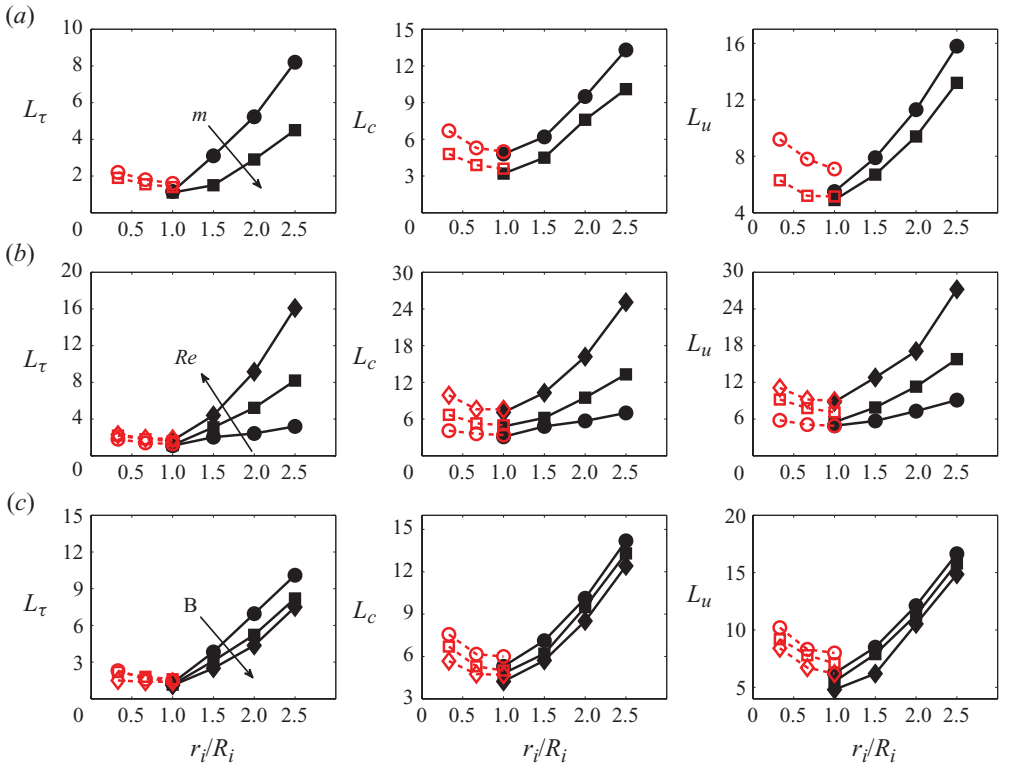


FIGURE 13. (Colour online) Variations in entry lengths with ratio r_i/R_i: (*a*) $m=1$ and $m=10$ for fixed $Re=20$, $B=10$; (*b*) $Re=5$, $Re=20$ and $Re=40$, for fixed $m=1$, $B=10$; (*c*) $B=5$, $B=10$ and $B=20$ for fixed $m=1$, $Re=20$. Each row (*a*)–(*c*) shows the three entry lengths: L_τ, L_c and L_u. Each figure consists of two sequences of simulations: $R_i=0.6$ with $r_i=0.2,\ 0.4,\ 0.6$ (contraction flows), and secondly $R_i=0.2$ with $r_i=0.2,\ 0.3,\ 0.4,\ 0.5$ (expansion flows).

although increases in entry length due to contraction are not very significant. It is interesting that for both the contraction and expansion series, the entry lengths are comparable at $r_i=R_i$, although these have quite different geometries and relative flow rates for the different series. Flows in which there is a significant expansion have the largest development lengths and also the largest differences between L_c and L_u, the latter is due to increased diffusion/dispersion in expansion flows, as illustrated and discussed earlier; see figure 12. As the diffuse layer becomes thicker, it is not possible for the velocity to become established before the concentration field is developed. For less diffuse interfaces, the lengths L_c and L_u are very similar. Variations with m, Re and B follow predictable qualitative trends. Increased m and B (within the range allowable to preserve the case 1 solutions) both increase the viscosity of the flow and decrease the entry lengths. Increasing Re has the effect of increasing entry lengths. Unlike duct flows of Newtonian fluids, the increase in entry length with Re is not linear.

4. Stability of the established flow

The stability of visco-plastically lubricated flows has been studied by Frigaard (2001) and Moyers-Gonzalez *et al.* (2004). Although Frigaard (2001) studies linear

https://doi.org/10.1017/S0022112010006348 Published online by Cambridge University Press

stability of plane channel flows, as opposed to pipe flows, we expect very similar results. In conducting linear stability studies of shear flows of yield stress fluids containing finite plug regions, one makes the (valid) assumption that the plug is not broken by the infinitesimal perturbation. This results in a decoupling of the linear stability into a sequence of reduced single-fluid stability problems, each formulated on a purely viscous shear layer. For these reduced problems, the length scales and velocity scales are smaller and we generally find that the linear stability is enhanced.

The linear stability results are of limited practical use unless the stability extends into the nonlinear regime. The only nonlinear study is that of Moyers-Gonzalez *et al.* (2004), who consider a parallel pipe flow similar to that considered here. For yield stress fluid flows, conducting weakly nonlinear stability analyses is problematic, since the topology of the yielded regions when perturbed is unknown, and therefore it is more common to use energy methods. In the flow considered here, there is the additional problem of the interface to deal with, which is not ideal for energy methods. However, in Moyers-Gonzalez *et al.* (2004), they circumvented these difficulties by assuming a finite stress perturbation that is small enough to leave a ring of unyielded fluid around the core. This ring of fluid may translate away from the concentric location, but as it remains unyielded the interface velocity is described as a function of the plug velocity. This enables application of the energy method and derivation of lower bounds on Re, for exponential decay of the velocity perturbation.

This hybrid type of analysis in Moyers-Gonzalez *et al.* (2004) does give stability for Re in the range 10–100, depending on the other parameters, but has a number of drawbacks. Firstly, the bounds are certainly conservative and also not particularly easy to evaluate numerically. Secondly, the decay predicted is in fact decay to a base solution that need not be axisymmetric. The experiments performed by Huen *et al.* (2007) showed that the flows achieved are axisymmetric, but this study did not look at flow stability. Questions of symmetry breaking remain therefore open, but in any case will not be answered here. Thirdly, unlike a weakly nonlinear stability analysis, no information on the flow structure is forthcoming from the energy method. In particular, we have no understanding of how the plug region influences stability of the flow. Lastly, we note that Moyers-Gonzalez *et al.* (2004) considered the $Pe \to \infty$ limit of the model analytically. However, we have seen earlier in §§ 2.3.2 and 3.1 that even with large Pe, strong dispersive effects can lead to modified flow structures.

Our stability analysis focuses on developing a finer understanding of the types of flows that occur when perturbing case 1 base flows. This is a temporal stability analysis conducted numerically on a spatially periodic cell. As well as the base flow parameters (m, B, r_i), the flows are characterised by Re and the axial periodicity of the flow. In conducting a numerical study, it is necessary to specify initial conditions for the perturbations and in the nonlinear regime the precise solution behaviour is influenced by the choice of initial conditions. Thus necessarily, what is presented are examples of flow behaviour rather than general results. In this sense, the study is complementary to that of Moyers-Gonzalez *et al.* (2004).

4.1. *Methodology*

Having fixed the base flow parameters (m, B, r_i) and computed the analytic base flow $W(r)$, we select an axial wavelength α, which defines the length of computational domain: $2\pi/\alpha$. Taking $(0, W(r))$ and a unit step in concentration C at r_i as initial conditions, we first run the transient computations until steady state to establish the numerical base flow. This is done imposing periodicity at the ends of the spatial domain.

https://doi.org/10.1017/S0022112010006348 Published online by Cambridge University Press

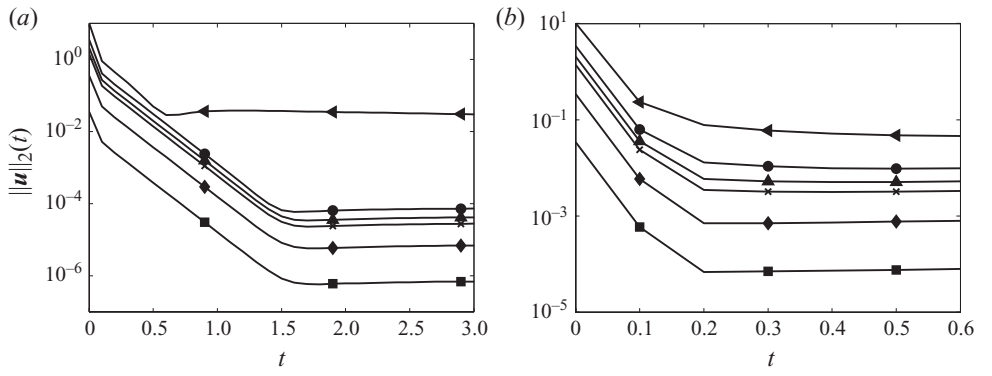


FIGURE 14. Decay of velocity perturbation for $r_i = 0.4$, $m = 10$, $B = 20$, at $Re = 1$: (*a*) case A; (*b*) case B. Different curves denote initial perturbation amplitudes: $A = 0.01$ (■), 0.1 (◆), 0.4 (×), 0.6 (▲), 1 (●), 3 (◀).

We then superimpose an initial condition on the numerical base flow and launch the transient computation. Initial conditions are selected to be spatially periodic (wavenumber α), to be divergence-free and to satisfy boundary, interface and symmetry conditions. Within this, we construct the radial dependence using polynomials of the lowest order possible. Additionally, we consider two types of initial perturbation: case A, where the entire domain is perturbed; case B, where only yielded regions of the flow domain are perturbed. These two initial perturbations are given in the form:

$$\boldsymbol{u}(r, z, 0) = A(v_r(r, z), v_z(r, z)); \qquad \|(v_r(r, z), v_z(r, z))\|_2 = \|W(r)\|_2, \tag{4.1}$$

so that A denotes the size of the L^2 norm of the initial perturbation, relative to that of the base flow, i.e. A^2 represents the relative kinetic energy of the initial perturbation. The spatial structure of these perturbations is described in the Appendix.

4.2. *Results*

For the results presented below, we have focused on two specific base flows. For both flows, we fix $(m, B) = (10, 20)$ and we consider $r_i = 0.4$ and $r_i = 0.6$. For both interface radii, there is a case 1 base solution. With $r_i = 0.4$, the yield surface is at $r_y \approx 0.71$ whereas for $r_i = 0.6$, the yield surface is at $r_y \approx 0.72$, resulting in a thinner plug. For both base solutions, we have performed stability studies for both case A and case B initial conditions, for $Re = 1,\ 10,\ 100,\ 1000$ and for amplitudes $A = 0.01,\ 0.1,\ 0.2,\ 0.4,\ 0.6,\ 0.8,\ 1,\ 2,\ 3$. Various additional computations have also been run to explore specific parameters, so that in total around 200 computations have been performed. For all results shown, we have fixed the wavenumber α so that the length of domain is $L = 2\pi/\alpha = 4$.

We start by exploring the decay of $\|\boldsymbol{u}\|_2(t)$ for different A at low Re and with the thicker plug, $r_i = 0.4$. The results are shown in figure 14 for cases A and B. For both cases, we see an initial very rapid drop in $\|\boldsymbol{u}\|_2(t)$, which we shall explore below. The case A perturbation shows a distinct linear profile (exponential decay) until a constant saturation value is obtained. For low amplitudes, the saturation values are very small. These values are limited anyway by the tolerance set in the nonlinear iteration for the solution. We see that for $A = 0.01$, we approach this tolerance. At higher A, the perturbation decays to a value in the range $\|\boldsymbol{u}\|_2(t) \sim O(10^{-4})$ for all except the largest A. For this level of error, the final solutions appear to the eye to be very close

https://doi.org/10.1017/S0022112010006348 Published online by Cambridge University Press

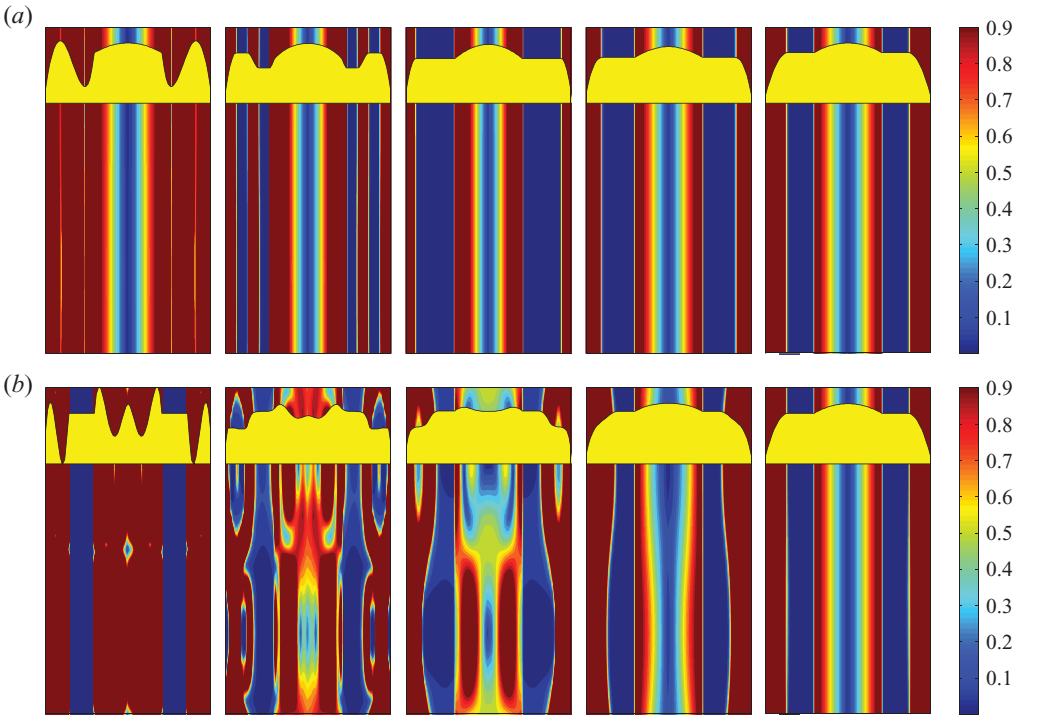


FIGURE 15. Initial stages of decay for amplitude $A = 0.4$ and for $r_i = 0.4$, $m = 10$, $B = 20$, at $Re = 1$. Each plot shows the magnitude of the strain rate at times (left to right) $t = 0$, $t = 0.001$, $t = 0.002$, $t = 0.005$ and $t = 1$, with superimposed axial velocity profile: (a) case A; (b) case B.

to the base solution and the error comes principally from diffusive/dispersive effects near the interface.

For the case B initial conditions, we see immediately that the decay is rapid, but that the final saturation values are not as small as for the case A initial conditions. There is a linear region of exponential decay, but it is apparently much shorter than for the case A perturbation. To explore this difference, we investigate the initial sudden decay of the perturbation. Figure 15 shows the strain rate magnitude (and superimposed velocity profile) for the 40 % amplitude perturbation with $r_i = 0.4$ at times $t = 0$, $t = 0.001$, $t = 0.002$, $t = 0.005$ and $t = 1$. Figure 15(a) shows the case A initial condition and figure 15(b) shows the case B initial condition.

It is interesting to note that for the case A initial condition, the plug reforms very quickly. For the case B initial condition, since the plug is not initially broken all the energy of the initial perturbation is localised in the core fluid and yielded part of the outer fluid. For $t > 0$, these large gradients dissipate rapidly, but in the process destroy the plug region. Both perturbations in fact decay to the same solution (see last plot at $t = 1$), but we observe that the case A perturbation has a reformed plug and quasi-1D flow structure much more rapidly. The longer time of decay allows for more diffusion and dispersion at the interface, so that the final values of the case B perturbations are larger than those of the case A perturbations.

Similar features are found with the $r_i = 0.6$ base solution, as shown in figure 16. This base solution has a thinner plug region and is expected to be less stable. We observe that the decay of $\|\boldsymbol{u}\|_2(t)$ is qualitatively similar to that at $r_i = 0.4$, but that

https://doi.org/10.1017/S0022112010006348 Published online by Cambridge University Press

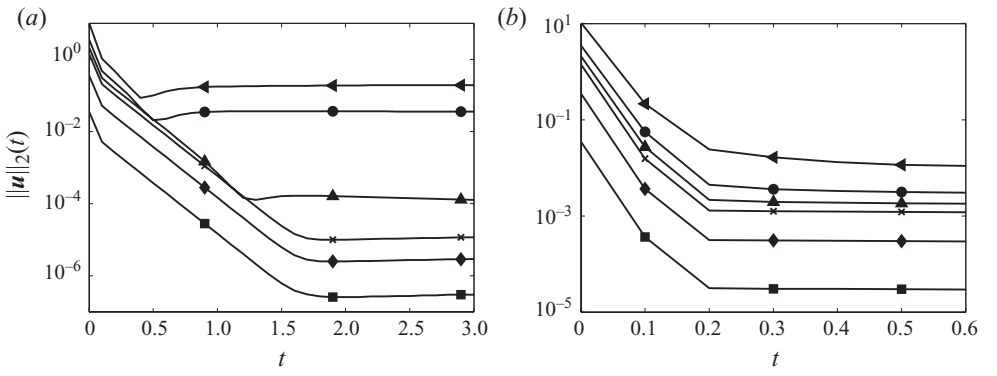


FIGURE 16. Decay of velocity perturbation for $r_i = 0.6$, $m = 10$, $B = 20$, at $Re = 1$: (*a*) case A; (*b*) case B. Different curves denote initial perturbation amplitudes: $A = 0.01$ (■), 0.1 (◆), 0.4 (×), 0.6 (▲), 1 (●), 3 (◀).

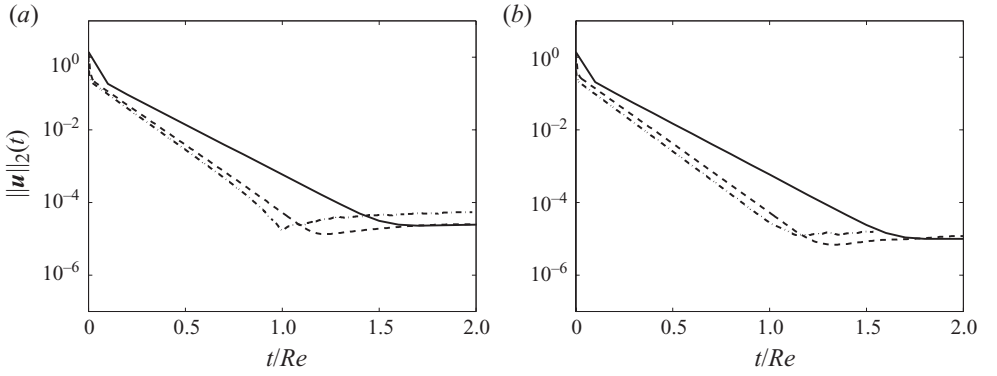


FIGURE 17. Decay of velocity perturbation for case A with $m = 10$, $B = 20$, $A = 0.4$, plotted against t/Re. Line styles (—), (– –) and (—·) denote $Re = 1$, $Re = 10$ and $Re = 100$ respectively. (*a*) $r_i = 0.4$; (*b*) $r_i = 0.6$.

the final values are larger. For final values greater than around 1 %, the final solutions are progressively different to the base flow, and we explore some of these secondary flows later.

As Re is increased, it is found that the time required for decay of $\|\boldsymbol{u}\|_2(t)$ to its saturation value is progressively longer. Figure 17 shows this decay as a function of t/Re for three different Re values. Although the curves do not collapse to a single curve, the scaling is evident and indicates that this intermediate stage is dominated by pure viscous decay. This makes sense since after the plug has formed (or reformed) and the flow is quasi-1D, the dissipation is governed by the viscous terms. Due to the viscosity ratio $m \neq 1$, there are in fact two viscous time scales and we should not be surprised that the curves do not collapse fully.

Figures 18 and 19 present a panorama of our computed results, in the form of colourmaps of $C(r, z, t)$ at $t = 9.9$ for varying A and Re. By this time, even for the larger Re, the flow structure is predictive of the final form. We show only the less stable case B initial perturbation. Figures 18 and 19 show the case B initial perturbation, for base flows $r_i = 0.4$ and $r_i = 0.6$, respectively. The overall pattern indicated by these figures is that for a wide range of A and Re, this flow is temporally stable to

https://doi.org/10.1017/S0022112010006348 Published online by Cambridge University Press

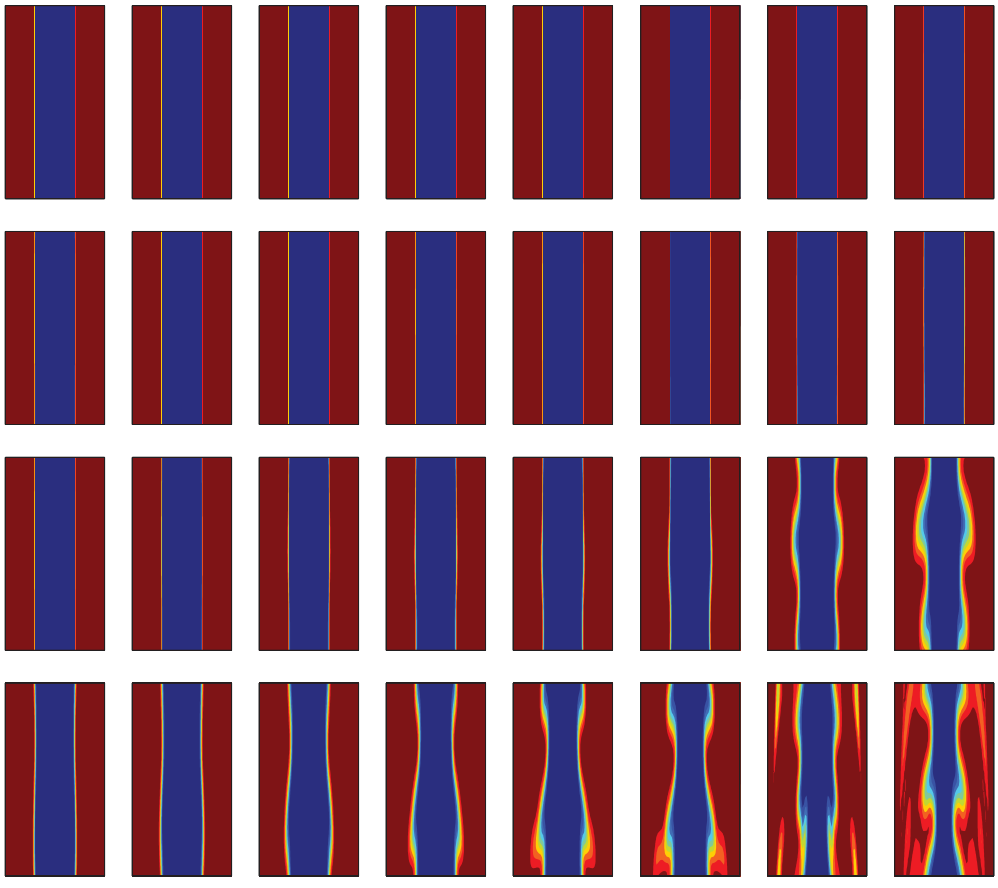


FIGURE 18. (Colour online) Concentration colourmaps for case B initial perturbation for $r_i = 0.4$ and $(m, B) = (10, 20)$, at $t = 9.9$. The rows from top to bottom show $Re = 1$, $Re = 10$, $Re = 100$ and $Re = 1000$. The columns, from left to right show the amplitudes: $A = 0.1,\ 0.2,\ 0.4,\ 0.6,\ 0.8,\ 1\ ,2,\ 3$.

axisymmetric perturbations. For $A \lesssim 1$ and $Re \lesssim 100$, we observe that the base flow is essentially recovered, with dispersive effects barely visible. However, as either speed (Re) or amplitude is increased, various secondary flow effects become evident. At very large Re and A, the flows are unstable and the fluids mix dispersively. We need to be cautious about the interpretation of some of these flows, as the numerical method has limited spatial resolution. Nevertheless, the onset of many of these flows, at lower Re and A, is undoubtedly physical, similar to the pearl and mushroom simulations of § 2.3.2.

We now look in more detail at some of the basic phenomena that we have seen in the sequence (figures 18 and 19). To start with, we observe that some of the plots in figures 18 and 19 show a wavy-walled interface at $t = 9.9$. For example, consider a case B initial perturbation with $r_i = 0.4$ for $Re = 100$ and with $A = 1$ (see figure 18, third row, sixth column). Figure 20 shows the magnitude of strain rate and the colourmaps at $t = 0$, $t = 0.2$, $t = 0.5$, $t = 0.8$, $t = 1.1$. We see that, as before, the initial dissipation of energy breaks the plug and results in a marked axial variation of the perturbation. The velocity perturbation decays in both the core fluid and in the outer fluid, but we can see that the interface is still deformed at the time at which the fluid at the

https://doi.org/10.1017/S0022112010006348 Published online by Cambridge University Press

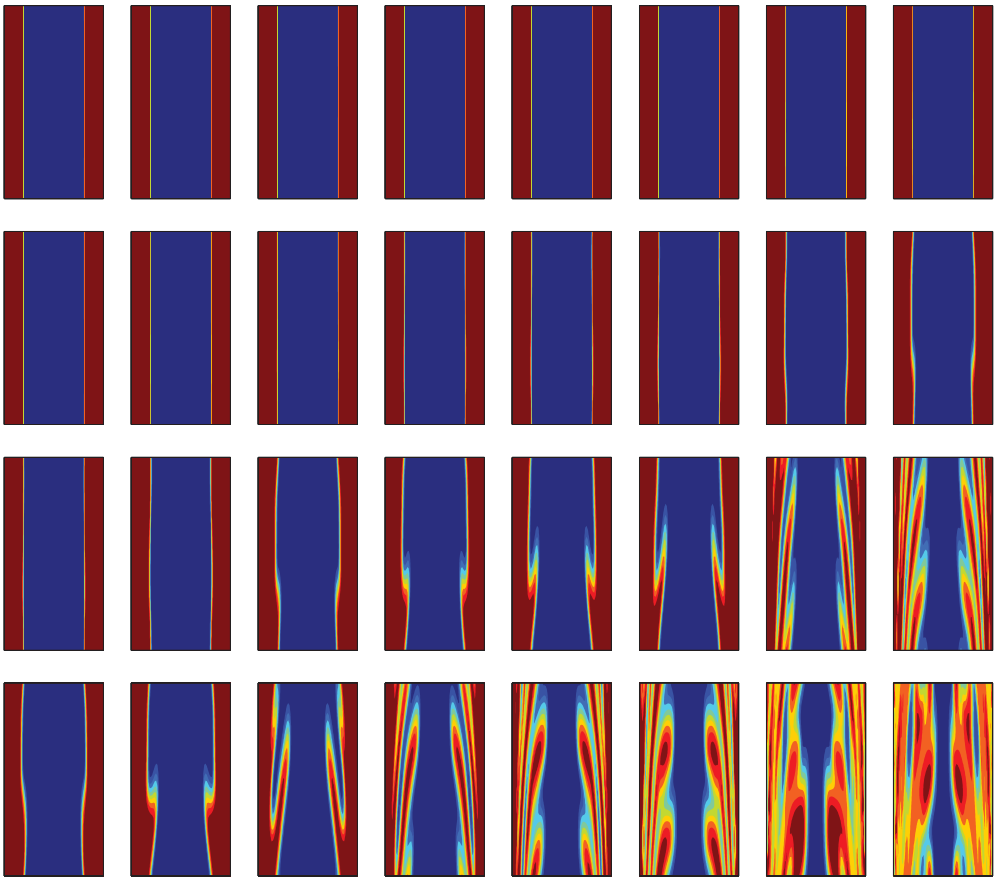


FIGURE 19. (Colour online) Concentration colourmaps for case B initial perturbation for $r_i = 0.6$ and $(m, B) = (10, 20)$, at $t = 9.9$. The rows from top to bottom show $Re = 1$, $Re = 10$, $Re = 100$ and $Re = 1000$. The columns, from left to right show the amplitudes: $A = 0.1,\ 0.2,\ 0.4,\ 0.6,\ 0.8,\ 1\ ,2,\ 3$.

interface becomes unyielded (between $t = 0.5$ and $t = 0.8$). The interface effectively freezes in whatever shape it is in at the point where the stress falls below the yield stress. Once frozen in, the interface retains its shape. We can see that at $t = 1.1$, the inner fluid velocity field is still perturbed by the shape of the interface, whereas that in the yielded part of the lubricating fluid is essentially axial. This is a first type of secondary flow that can be found.

On increasing the initial perturbation amplitude, the wavy nature of the interface is increased and eventually we develop secondary flows that break through the surrounding plug, at places. These flows have partly unyielded plugs and interfacial patterns that are similar to the pearl patterns of d'Olce (2008) and d'Olce *et al.* (2008). An example is shown in figure 21. We note that the pearl-like flow structures observed are not permanent when the plug is yielded in parts. The uneven interfacial region means that there are 2D secondary flows present. Over time, these disperse the intermediate concentrations and numerical diffusion smooths the concentrations. An example of the long time evolution is shown in the final frame of figure 21, at $t = 100$.

For larger $r_i = 0.6$ (when the plug region is also narrower), the flows are less stable and the plug breaks at smaller amplitudes. An example is shown in figure 22. The flow

https://doi.org/10.1017/S0022112010006348 Published online by Cambridge University Press

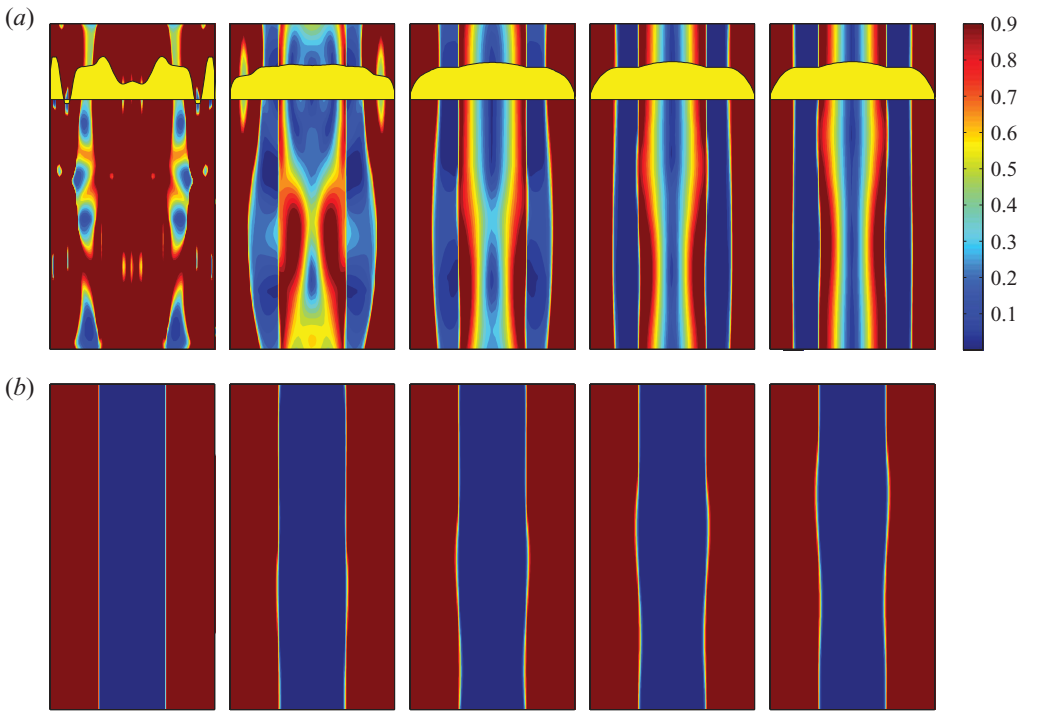


FIGURE 20. Freezing in of wavy-walled interfaces for a case B initial condition at $(m, B) = (10, 20)$ with $r_i = 0.4$, $A = 1$ and $Re = 100$. The plots are shown at $t = 0.2$, $t = 0.5$, $t = 0.8$, $t = 1.1$, $t = 1.4$ (left to right): (a) strain rate magnitude; (b) concentration.

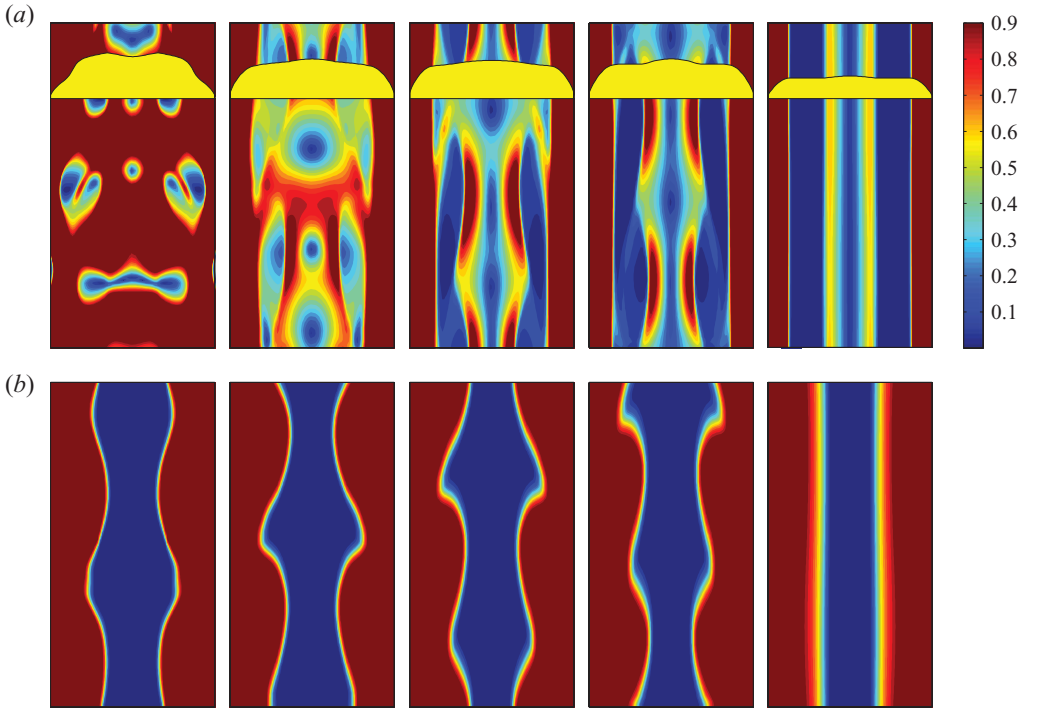


FIGURE 21. Pearl-like instabilities for a case B initial condition at $(m, B) = (10, 20)$ with $r_i = 0.4$, $A = 3$ and $Re = 100$. The plots are shown at $t = 0.7$, $t = 1.2$, $t = 1.7$, $t = 2.3$, $t = 100$ (left to right): (a) strain rate magnitude; (b) concentration.

https://doi.org/10.1017/S0022112010006348 Published online by Cambridge University Press

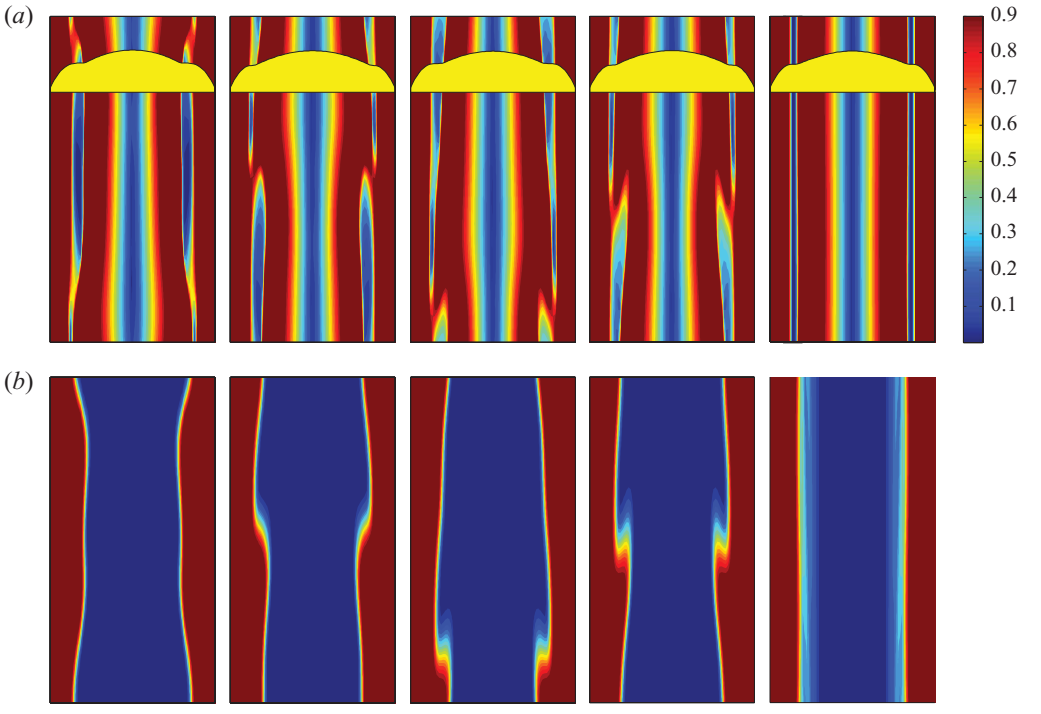


FIGURE 22. Pearl-like instabilities for a case B initial condition at $(m, B) = (10, 20)$ with $r_i = 0.6$, $A = 0.8$ and $Re = 100$. The plots are shown at $t = 2$, $t = 4$, $t = 6$, $t = 7$, $t = 100$ (left to right): (*a*) strain rate magnitude; (*b*) concentration.

patterns at intermediate times resemble the mushroom patterns of d'Olce (2008) and d'Olce *et al.* (2008). Again, at long times, numerical diffusion and physical dispersion dominate to render the flow axial with a significant mixed interfacial region.

5. Discussion

This paper has mostly focused on trying to understand better the stability and robustness of visco-plastically lubricated pipe flows. In the first place, we have shown that for wide ranges of operating parameters (Re, R_i), as long as the base flow parameters (m, B, r_i) admit a case 1 solution, then this base flow can be achieved by a start-up procedure analogous to that used experimentally by Huen *et al.* (2007). In contrast, for Newtonian multi-layer flows in similar configurations, both the experimental work of d'Olce (2008) and d'Olce *et al.* (2008) and our test computations presented in § 2.3.2 showed that many of these flows are convectively unstable leading to pearl and mushroom patterns. Even when convectively stable, we have been able to excite these patterns with relatively low-amplitude oscillations of the flow rate. In contrast, we have observed no signs of absolute instability in the start up of our flows, which are established as soon as the convectively unstable frontal region exits the pipe. This is perhaps the first indication of the robustness of the flows we have studied.

Secondly, we have carried out a parametric investigation of the entry length for establishment of the base flow. The entry length increases with Re, and decreases with

https://doi.org/10.1017/S0022112010006348 Published online by Cambridge University Press

m and B, as is intuitive. Note that the decrease with m is artificial in that we have scaled with the plastic viscosity of the lubricating fluid, as opposed to some average (plastic) viscosity. This means that the average viscosity always increases with m. The behaviour with r_i/R_i being minimal when the inlet radius matches the far-field radius is also intuitive. It is surprising that relatively few radii are needed to establish the flow.

Turning now to the flow stability, we have examined perturbations of two different flows with two different initial conditions, over a broad range of initial amplitudes A and Re. For $Re < 100$, we have routinely found stable flows for amplitudes $A \lesssim 1$. While this does not establish any theoretical limits, it does suggest that the analytic results in Moyers-Gonzalez *et al.* (2004) may be fairly conservative, especially since we have demonstrated that stability may result even when the base flow plug region is perturbed. Retaining an unyielded plug region was an essential part of the analysis in Moyers-Gonzalez *et al.* (2004).

At larger perturbation amplitudes, we have shown that there are interesting flow regimes that may result from perturbation of the base flow. For example, we are able to 'freeze in' the non-planar interface and form interesting non-Newtonian pearl and mushroom patterns. At still larger perturbations, large-scale dispersion occurs and some judgement needs exercising about the validity of the observed results in these regimes. Nevertheless, we have seen that even when significant mixing occurs, the perturbations often decay back to stable states.

We have also studied the nature of the energy decay when the flow is stable. There exists a significant and very fast transient in the initial stages, which is responsible for breaking and reforming of the plug. Presumably, this process is governed by the yield stress, whereas at later times, the decay is exponential and characteristically viscous. It is well known that yield stress fluids can have a finite time decay when stable, e.g. Glowinski (1983) and Zhang, Vola & Frigaard (2006). The typical result is proven by considering the energy decay, and involves a global bound on the decay of $\|\boldsymbol{u}\|_2$. This bound is exponential when the base flow is non-trivial, but occurs in finite time otherwise. It could be that for complex flows such as this, we may have more rapid decay than exponential, but only locally.

Much of our study has been targeted at verifying analytical stability results and exploring these flow features. An alternative approach would have been to use the computational solutions to compare against the experimental results in Huen *et al.* (2007). This comparison is hard to make at a quantitative level for a number of reasons. Firstly, the fluids used in Huen *et al.* (2007) (Carbopol and Xanthan solutions) are not well-represented by Bingham and Newtonian constitutive models, due to shear-thinning, so that the present computational model would need extending. Secondly, the experiments in Huen *et al.* (2007) were not particularly detailed, with only bulk quantities being measured. Principally, this was the interface radius, which did compare favourably with the 1D (base flow) design model used by Huen *et al.* (2007). If we were to extend this experimental study to compare directly against numerical solutions, we would certainly improve the visualisation aspects of Huen *et al.* (2007) to allow more detailed comparisons to be made.

Finally, we must acknowledge some restrictions on the study. Firstly and most importantly, the computations are axisymmetric. Such flows and perturbations can be significantly more stable than asymmetric perturbations. Having said this, we note that the experimental flows in Huen *et al.* (2007) were also observed to be axisymmetric. We suspect that the study of three-dimensional (3D) flows and instabilities will decrease the critical Reynolds numbers and amplitudes of perturbation, but that the

https://doi.org/10.1017/S0022112010006348 Published online by Cambridge University Press

flow will remain nonlinearly stable for practically significant ranges. To gain some insight into possible asymmetry effects, we are presently studying analogous flows in a plane channel.

A second restriction of our study is not exploring wavelength dependence of the nonlinear perturbations, instead keeping $\alpha = O(1)$ and fixed. In the Newtonian context, the long and short wavelength limits are often studied because of analytical simplifications of the linear stability problem, but here the linear stability problem is anyway stable to high Re, so that there is little benefit here. Another interest is in considering capillary effects, particularly at short wavelengths, but here these are absent due to the miscibility of the fluids. Even if we were to consider immiscible fluids, for typical experimental geometries and fluid properties ($\hat{R}$ in the range 0.01–0.1 m and yield stresses $\hat{\tau}_Y \gtrsim 1$ Pa), capillary effects are only significant by comparison to the yield stress at extremely small wavelengths and in initial perturbations that break the plug. Thus, we feel that $\alpha = O(1)$ is the most practically relevant range, although we acknowledge that a further study could be interesting.

Lastly, we have not considered convective stability explicitly (except in the sense that the frontal region of the start-up flows is convectively unstable). Partly, the reason for this is that we focus on case 1 flows for which the objective is to establish a stable multi-layer configuration. Once established, in all the usual multi-layer applications, one would be avoiding introduction of entry perturbations as far as possible. Nevertheless, our studies have shown that interesting convective effects may be frozen into the interface. This opens up interesting areas for application. This is therefore a second area that we are exploring in a more systematic fashion.

Financial support of the Natural Sciences and Engineering Research Council of Canada (NSERC) is gratefully acknowledged. We thank Dr D. Grecov for use of computational resources funded by the Canada Foundation for Innovation (CFI). We thank D. Vola and A. Wachs for their guidance in using PELICANS during the early part of this work. We thank the reviewers for their interesting comments.

Appendix. Equations of imposed perturbation

Initial conditions for the velocity perturbation $\boldsymbol{u}$ are constructed so as to satisfy the continuity equation and the various boundary and interface conditions. We consider two different cases, A and B. In case A, initially the whole domain is perturbed. In case B, the plug region is left intact by the initial perturbation. In both cases, we denote the initial velocity perturbation by $\boldsymbol{u}(r, z, 0) = A(v_r(r, z), v_z(r, z))$, where v_r and v_z are shape functions for the radial and axial components of the perturbed velocity, respectively and A is the amplitude of the perturbation. The components v_r and v_z can be defined in terms of a stream function ψ:

$$v_r = \frac{1}{r}\frac{\partial \psi}{\partial z}, \quad v_z = -\frac{1}{r}\frac{\partial \psi}{\partial r}. \tag{A 1}$$

We assume that ψ has the following form:

$$\psi = \zeta \{\phi(r)\sin(\alpha z) + f(r)\}, \tag{A 2}$$

where the length of the pipe section is $2\pi/\alpha$ and ζ is defined so as to normalise the perturbation with the base flow:

$$\zeta = \frac{\|W(r)\|_2}{\|(v_r(r, z), v_z(r, z))\|_2}. \tag{A 3}$$

https://doi.org/10.1017/S0022112010006348 Published online by Cambridge University Press

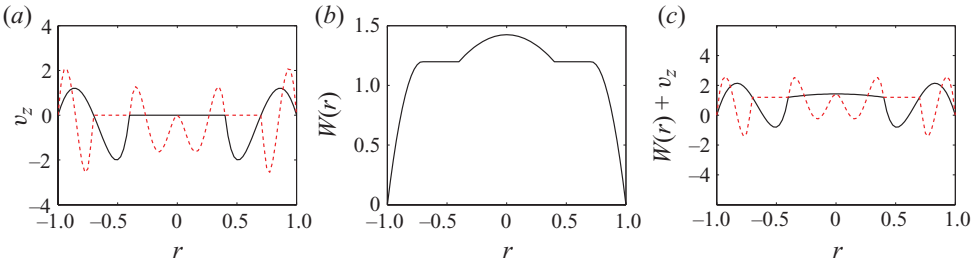


FIGURE 23. (Colour online) Example of the axial component of the initial velocity perturbations for $(m, B) = (10, 20)$ with $r_i = 0.4$, $A = 1$, plotted, where $\sin \alpha z = 1$: (*a*) axial component of initial velocity perturbations (solid line, case A; broken line, case B); (*b*) base flow; (*c*) superposition of perturbation and base flow.

A.1. Case A

We satisfy the following boundary conditions and continuity of stress and velocity at interface:

(i) at $r = 0$, $v_r = 0$, $\dfrac{\partial v_z}{\partial r} = 0$, $\psi = 0$,
(ii) at $r = r_i$, $\dot{\gamma}_{rr} = 0$, $\dot{\gamma}_{zz} = 0$, $\dot{\gamma}_{\theta\theta} = 0$, $\psi = 0$,
(iii) at $r = 1$, $v_r = 0$, v_z, $\psi = 0$.

For $r \leqslant r_i$, we have:

$$v_r = -\zeta r^3 (r - r_i)^3 \alpha \cos \alpha z, \tag{A 4}$$

$$v_z = \zeta [r^2 (r - r_i)^2 (7r - 4r_i) \sin \alpha z + 4r^2 (r - r_i)^2 + 2r^3 (r - r_i)], \tag{A 5}$$

and for $r > r_i$:

$$v_r = -\zeta \frac{(r - r_i)^3 (r - 1)^2 \alpha \cos \alpha z}{r}, \tag{A 6}$$

$$v_z = \zeta \left(\frac{(r - 1)(r - r_i)^2 (5r - 2r_i - 3)}{r} \sin \alpha z + \frac{2(r - 1)(r - r_i)(2r - r_i - 1)}{r} \frac{2mr_i^4 - Br_i^2/r_y - Br_i}{2(r_i - 1)^2} \right). \tag{A 7}$$

A.2. Case B

To keep the plug intact, we apply the following conditions:

(i) at $r = 0$, $v_r = 0$, $\dfrac{\partial v_z}{\partial r} = 0$, $\psi = 0$,
(ii) $r \in [r_i, r_y]$, $v_r = v_z = 0$, $\psi = 0$,
(iii) at $r = 1$, $v_r = v_z = 0$, $\psi = 0$.

For $r \leqslant r_i$, we have:

$$v_r = -\zeta r^3 (r - r_i)^2 \alpha \cos \alpha z, \tag{A 8}$$

$$v_z = \zeta r^2 (r - r_i)(6r - 4r_i) \sin \alpha z. \tag{A 9}$$

For $r > r_i$:

$$v_r = -\zeta \frac{(r - r_y)^2 (r - 1)^2 \alpha \cos \alpha z}{r}, \tag{A 10}$$

https://doi.org/10.1017/S0022112010006348 Published online by Cambridge University Press

$$v_z = \zeta \frac{2(r-1)(r-r_y)(2r-r_y-1)\sin\alpha z}{r}. \tag{A 11}$$

Figure 23 shows an illustrative example of axial components of the two initial velocity perturbations (case A and case B) and their superposition with the base flow velocity profile.

REFERENCES

Allouche, M., Frigaard, I. A. & Sona, G. 2000 Static wall layers in the displacement of two visco-plastic fluids in a plane channel. *J. Fluid Mech.* **424**, 243–277.

Bakhtiyarov, S. & Siginer, D. A. 1996 Fluid displacement in a horizontal tube. *J. Non-Newtonian Fluid Mech.* **65**, 1–15.

Balasubramaniam, R., Rashidnia, N., Maxworthy, T. & Kuang, J. 2005 Instability of miscible interfaces in a cylindrical tube. *Phys. Fluids* **17**, 052103.

Bercovier, M. & Engleman, M. 1980 A finite element method for incompressible non-Newtonian flows. *J. Comput. Phys.* **36**, 313–326.

Brezzi, F. & Fortin, M. 1991 *Mixed and Hybrid Finite Element Method.* Springer Series in Computational Mathematics, vol. 15. Springer.

Burghelea, T., Wielage-Burchard, K., Frigaard, I. A., Martinez, D. M. & Feng, J. 2007 A novel low inertia shear flow instability triggered by a chemical reaction. *Phys. Fluids* **19**, 083102.

Charru, F. 1998 'Phase diagram' of interfacial instabilities in two-layer shear flows. In *Proceedings of the Third International Conference on Multiphase Flow, ICMF'98*, Lyon, France, June 8–12, 1998.

Charru, F. & Hinch, E. J. 2000 'Phase diagram' of interfacial instabilities in a two-layer Couette flow and mechanism of the long wave instability. *J. Fluid Mech.* **414**, 195–223.

Chen, C.-Y. & Meiburg, E. 1996 Miscible displacements in capillary tubes. Part 2. Numerical simulations. *J. Fluid Mech.* **326**, 57–90.

Ern, P., Charru, F. & Luchini, P. 2003 Stability analysis of a shear flow with strongly stratified viscosity. *J. Fluid Mech.* **496**, 295–312.

Frigaard, I. A. 2001 Super-stable parallel flows of multiple visco-plastic fluids. *J. Non-Newtonian Fluid Mech.* **100**, 49–76.

Frigaard, I. A., Howison, S. D. & Sobey, I. J. 1994 On the stability of Poiseuille flow of a Bingham fluid. *J. Fluid Mech.* **263**, 133–150.

Frigaard, I. A. & Nouar, C. 2005 On the usage of viscosity regularisation methods for visco-plastic fluid flow computation. *J. Non-Newtonian Fluid Mech.* **127**, 1–26.

Frigaard, I. A., Scherzer, O. & Sona, G. 2001 Uniqueness and non-uniqueness in the steady displacement of two viscoplastic fluids. *Z. Angew. Math. Mech.* **81** (2), 99–118.

Gabard, C. 2001 Etude de la stabilité de films liquides sur les parois d'une conduite verticale lors de l'ecoulement de fluides miscibles non-Newtoniens. These de l'Universite Pierre et Marie Curie (PhD thesis), Orsay, France.

Gabard, C. & Hulin, J.-P. 2003 Miscible displacements of Non-Newtonian fluids in a vertical tube. *Eur. Phys. J.* E **11**, 231–241.

Glowinski, R. 1983 *Numerical Methods for Nonlinear Variational Problems.* Springer.

Glowinski, R. & Le Tallec, P. 1989 *Augmented Lagrangian and Operator-Splitting Methods in Nonlinear Mechanics.* SIAM.

Glowinski, R., Lions, J. L. & Tremolieres, R. 1976 *Analyse Numérique des Inéquations Variationelles,* vol. 2. Dunod. (English version: 1981 *Numerical Analysis of Variational Inequalities.* North-Holland.)

Govindarajan, R. 2004 Effect of miscibility on the linear instability of two-fluid channel flow *Intl J. Multiphase Flow* **30**, 1177–1192.

Goyal, N. & Meiburg, E. 2006 Miscible displacements in Hele–Shaw cells: two-dimensional base states and their linear stability. *J. Fluid Mech.* **558**, 329–355.

Goyal, N., Pichler, H. & Meiburg, E. 2007 Variable density, miscible displacements in a vertical Hele–Shaw cell: linear stability. *J. Fluid Mech.* **584**, 357–372.

https://doi.org/10.1017/S0022112010006348 Published online by Cambridge University Press

Hickox, C. E. 1971 Instability due to viscosity and density stratification in axisymmetric pipe flow. *Phys. Fluids* **14** (2), 251–262.

Hinch, E. J. 1984 A note on the mechanism of the instability at the interface between two shearing fluids. *J. Fluid Mech.* **114**, 463–465.

Hooper, A. P. & Boyd, W. G. 1987 Shear flow instability due to a wall and a viscosity discontinuity at the interface. *J. Fluid Mech.* **179**, 201–225.

Huen, C. K., Frigaard, I. A. & Martinez, D. M. 2007 Experimental studies of multi-layer flows using a visco-plastic lubricant. *J. Non-Newtonian Fluid Mech.* **142**, 150–161.

Joseph, D. D., Bai, R., Chen, K. P. & Renardy, Y. Y. 1997 Core–annular flows. *Annu. Rev. Fluid Mech.* **29**, 65–90.

Joseph, D. D. & Renardy, Y. Y. 1993 *Fundamentals of Two-Fluid Dynamics*. Interdisciplinary Applied Mathematics Series. Springer.

Khomami, B. 1990 Interfacial stability and deformation of two stratified power law fluids in plane Poiseuille flow. Part 1. Stability analysis. *J. Non-Newtonian Fluid Mech.* **36**, 289–303.

Kuang, J., Maxworthy, T. & Petitjeans, P. 2003 Miscible displacements between silicone oils in capillary tubes. *Eur. J. Mech.* B **22**, 271–277.

Lajeunesse, E. 1999 Déplacement et instabilités de fluides miscibles et immiscibles en cellules de Hele-Shaw. These de l'Universite Pierre et Marie Curie (PhD thesis), Orsay, France.

Lajeunesse, E., Martin, J., Rakotomalala, N. & Salin, D. 1997 3D Instability of miscible displacements in a Hele–Shaw cell. *Phys. Rev. Lett.* **79**, 5254–5257.

Lajeunesse, E., Martin, J., Rakotomalala, N. & Salin, D. 2001 The threshold of the instability in miscible displacements in a Hele–Shaw cell at high rates. *Phys. Fluids* **13** (3), 799–801.

Lajeunesse, E., Martin, J., Rakotomalala, N., Salin, D. & Yortsos, Y. 1999 Miscible displacement in a Hele–Shaw cell at high rates. *J. Fluid Mech.* **398**, 299–319.

LeVeque, R. 2002 *Finite Volume Methods for Hyperbolic Problems*. Cambridge Texts in Applied Mathematics. Cambridge University Press.

Moyers-Gonzalez, M. A., Frigaard, I. A. & Nouar, C. 2004 Nonlinear stability of a visco-plastically lubricated viscous shear flow. *J. Fluid Mech.* **506**, 117–146 .

Nouar, C., Kabouya, N., Dusek, J. & Mamou, M. 2007 Modal and non-modal linear stability of the plane Bingham–Poiseuille flow. *J. Fluid Mech.* **577**, 211–239.

d'Olce, M. 2008 Instabilités de cisaillement dans lécoulement concentrique de deux fluides miscibles These de l'Université Pierre et marie Curie (PhD thesis), Paris, France.

d'Olce, M., Martin, J., Rakotomalala, N. & Salin, D. 2008 Pearl and mushroom instability patterns in two miscible fluids core–annular flows. *Phys. Fluids* **20**, 024104.

d'Olce, M., Martin, J., Rakotomalala, N., Salin, D. & Talon, L. 2009 Convective/absolute instability in miscible core–annular flow. Part 1. Experiments. *J. Fluid Mech.* **618**, 305–322.

Petitjeans, P. & Maxworthy, T. 1996 Miscible displacements in capillary tubes. Part 1. Experiments. *J. Fluid Mech.* **326**, 37–56.

Pinarbasi, A. & Liakopoulos, A. 1995 Stability of two-layer Poiseuille flow of Carreau–Yasuda and Bingham-like fluids. *J. Non-Newtonian Fluid Mech.* **57**, 227–241.

Papanastasiou, T. 1987 Flows of materials with yield. *J. Rheol.* **31**, 385–404.

Quarteroni, A. & Valli, A. 2008 *Numerical Approximation of Partial Differential Equations*. Springer Series in Computational Mathematics, vol. 23. Springer.

Rakotomalala, N., Salin, D. & Watzky, P. 1997 Miscible displacement between two parallel plates: BGK lattice gas simulations. *J. Fluid Mech.* **338**, 277–297.

Ranganathan, T. & Govindarajan, R. 2001 Stabilization and destabilization of channel flow by location of viscosity-stratified fluid layer. *Phys. Fluids* **13**, 1–3.

Sahu, K. C., Ding, H., Valluri, P. & Matar, O. M. 2009*a* Pressure- driven miscible two-fluid channel flow with density gradients. *Phys. Fluids* **21**, 043603.

Sahu, K. C., Ding, H., Valluri, P. & Matar, O. M. 2009*b* Linear stability analysis and numerical simulation of miscible two-layer channel flow. *Phys. Fluids* **21**, 042104.

Scoffoni, J., Lajeunesse, E. & Homsy, G. M. 2001 Interfacial instabilities during displacemnts of two miscible fluids in a vertical pipe. *Phys. Fluids* **13** (3), 553–556.

Selvam, B., Merk, S., Govindarajan, R. & Meiburg, E. 2007 Stability of miscible core–annular flow with viscosity stratification. *J. Fluid Mech.* **592**, 23–49.

https://doi.org/10.1017/S0022112010006348 Published online by Cambridge University Press

Selvam, B., Talon, L., Leshafft, L. & Meiburg, E., 2009 Convective/absolute instability in miscible core–annular flow. Part 2. Numerical simulations and nonlinear global modes. *J. Fluid Mech.* **618**, 323–348.

Shariati, M., Talon, L., Martin, J., Rakotomala, N., Salin, D. & Yortsos, Y. C. 2004 Fluid displacement between two parallel plates: a non-empirical model displaying change of type from hyperbolic to elliptic equations *J. Fluid Mech.* **519**, 105–132.

Su, Y. Y. & Khomami, B. 1991 Stability of multi-layer power law and second order fluids in plane Poiseuille flow. *Chem. Engng Commun.* **109**, 209–223.

Taghavi, S. M., Seon, T., Martinez, D. M. & Frigaard, I. A. 2009 Buoyancy-dominated displacement flows in near-horizontal channels: the viscous limit. *J. Fluid Mech.* **639**, 1–35.

Talon, L., Martin, J., Rakotomala, N., Salin, D. & Yortsos, Y. C. 2004 Crossing the elliptic region in a hyperbolic system with change-of-type behavior arising in flow between two parallel plates *Phys. Rev.* E **69**, 066318.

Waters, N. D. 1983 The stability of two stratified power law fluids in Couette flow. *J. Non-Newtonian Fluid Mech.* **12**, 85–94.

Waters, N. D. & Keeley, A. M. 1987 The stability of two stratified non-Newtonian liquids in Couette flow. *J. Non-Newtonian Fluid Mech.* **24**, 161–181.

Wesseling, P. 2001 *Principles of Computational Fluid Dynamics*. Springer Series in Computational Mathematics, vol. 29. Springer.

Yang, Z. & Yortsos, Y. C. 1997 Asymptotic solutions of miscible displacements in geometries of large aspect ratio. *Phys. Fluids* **9** (2), 286–298.

Yiantsos, S. G. & Higgins, B. G. 1988 Linear stability of plane Poiseuille flow of two superposed fluids. *Phys. Fluids* **31**, 3225–3238.

Yih, C.-S. 1967 Instability due to viscosity stratification. *J. Fluid Mech.* **27** (2), 337–352.

Zhang, J., Vola, D. & Frigaard, I. A. 2006 Yield stress effects on Rayleigh–Benard convection. *J. Fluid Mech.* **566**, 389–419.

https://doi.org/10.1017/S0022112010006348 Published online by Cambridge University Press